

RESEARCH ARTICLE

WILEY

Development of a passive-adaptive slat for a wind turbine airfoil

 Florian N. Schmidt  | Jochen Wild 

Institute of Aerodynamics and Flow Technology, DLR - German Aerospace Center, Braunschweig, Germany

Correspondence

Florian N. Schmidt, Institute of Aerodynamics and Flow Technology, DLR - German Aerospace Center, Braunschweig 38108, Germany.

Email: f.schmidt@dlr.de

Funding information

German Ministry of Economic Affairs and Energy (BMWi), Grant/Award Number: 0324032D; German Parliament

Abstract

A passive-adaptive slat concept was designed to avoid separation in the root region of a horizontal-axis wind turbine blade. This concept incorporates an autonomously moveable slat device only driven by the aerodynamic forces acting on it without the need for mechanical or electrical actuation. It opens at high local angles of attack to delay the stall angle and closes for small angles of attack to increase the lift to drag ratio of the blade segment. This article describes the development of a passive-adaptive slat for a DU-91-W2-250 airfoil, which is a segment of the reference rotor blade in the project SmartBlades 2.0. In the course of the passive-adaptive slat design, the optimization of the slat and its extended position is presented. This is followed by the development of two passive-adaptive slat kinematics, which are opening and closing the slat passively at different angles of attack. With the designed passive-adaptive slat the stall of the airfoil is delayed by 20° in incidence and the maximum lift of the airfoil is increased by about 130% at the same time in comparison to the original airfoil. Furthermore, the DU-91-W2-250 airfoil with moveable passive-adaptive slat has in most conditions a higher climb index and therefore a better aerodynamic performance than the same airfoil with a fixed integrated slat.

KEYWORDS

high-lift system, optimization, passive stall control, passive-adaptive slat kinematics, rotor blade slat, wind energy

1 | INTRODUCTION

The root sections of commercial wind turbines often operate with separation on the upper blade surface due to stalled flow caused by their non-aerodynamic design. The separated flow in combination with a fluctuating wind field induces fluctuating loads on the rotor blade, which cause a reduction of the blade's lifetime and efficiency.¹ To extend the blade lifetime and to improve its performance, the flow separation in the root section needs to be avoided. Currently, there is a wide field of research to reduce the flow separation as well as the loads on a rotor blade with the help of passive and active flow control systems.²⁻⁵ In commercial wind turbines vortex generators (VGs) are mainly used for this purpose for decades. VGs are aerodynamical devices, which cause the formation of longitudinal vortices. The vortices lead to further mixing of the downstream flow and transport momentum from the outer flow to the near wall region.^{6,7} Hereby, the boundary layer flow is refreshed by flow with higher kinetic energy, which stabilizes it more against separation in an adverse pressure gradient. It has been successfully demonstrated that they can be used to shift the stall of a wind turbine airfoil towards higher angles of attack (α).^{8,9} Øye¹⁰ has shown that the power performance of a

This is an open access article under the terms of the Creative Commons Attribution-NonCommercial-NoDerivs License, which permits use and distribution in any medium, provided the original work is properly cited, the use is non-commercial and no modifications or adaptations are made.

© 2021 Deutsche Zentrum für Luft- und Raumfahrt. Wind Energy on published by John Wiley & Sons Ltd.

wind turbine can be significantly improved by retrofitting rotor blades with VGs. At the same time, VGs cause a slight increase in drag,¹¹ and their effective range is limited as long as the separation is downstream. In contrast, it is known from aircraft design that slats allow a much wider range of application of an airfoil with respect to the angle of attack range.¹²

For this reason, Zahle et al¹³ designed a rigid slat for a 40% thick flatback airfoil and investigated the geometry both numerically and experimentally. The investigations showed that the maximum lift of the wind turbine airfoil can be increased by more than 130% due to a stall incidence increase by up to 16° with the help of a slat. Pechlivanoglou et al¹⁴ obtained a maximum lift increase by more than 75% in comparable investigations based on wind tunnel measurements on a thick wind turbine airfoil with a rigid slat. They also demonstrated with simulations using the Blade Element Momentum (BEM) theory that a gain in power generation of 0.5–1% can be realized with the use of their slat device. Gaunaa et al¹⁵ have shown as well that installing a rigid slat and therefore avoiding separation by delaying the stall in the root section of a wind turbine blade could lead to an annual energy production increase by up to 1%.

Manso Jaume and Wild¹⁶ demonstrated a large potential of stall delay by designing an auxiliary and an integrated rigid slat for a thick wind turbine airfoil with the help of an aerodynamic optimization procedure using CFD simulations. Especially the designed two-element airfoil with the integrated rigid slat shows a high stall delay, a high lift after stall, and a higher aerodynamic efficiency than the original airfoil without a slat device. Their integrated version of the slat is also the starting point of the present study. Later, Steiner et al¹⁷ pointed out that the aerodynamic performance of a rotor blade with a rigid slat can be even more increased, when the rigid slat and the main airfoil are designed together.

On the one hand, slats improve the aerodynamic performance of a blade section at high local angles of attack by delaying the stall, but on the other hand, an airfoil with an open slat shows a lower lift to drag ratio compared to the same airfoil with a retracted slat for small angles of attack.¹⁸ Since the local angle of attack could suddenly change because of the fluctuating wind field, the slat of a wind turbine blade should be moveable with reference to the inflow.

Singh et al¹⁹ have tested in a wind tunnel experiment, whether the slat designed by Manso Jaume and Wild¹⁶ can reduce the dynamic loads on a wind turbine airfoil based on the DU-91-W2-250, when actively controlled. The active slat is shape-adaptive with the help of an actively deformable trailing edge, which is used to vary the gap between the slat and the main airfoil. The airfoil with the active slat was exposed to different complex inflows with varying fluctuation. According to Singh et al., the active slat can reduce fluctuating loads up to 59% for low frequency gust inflows. However, in some cases, where the active slat regulation could not adapt to the incoming flow, the active regulation amplified the loads on the airfoil. The use of such an active slat for stall delay and load reduction is accordingly possible but very dependent on the correct control strategy. The problem with such an active control system is that it causes extra maintenance work, when it is used at a wind turbine. Furthermore, when the actuation of such an active flow control device is designed with the use of an electrical system, the device and its regulation systems need sufficient lightning protection. The advantages of using a slat device should therefore be exploited without using any complex control system.

The aim of the presented research is to develop a moveable slat for the root section of a rotor blade based on the integrated slat concept of Manso Jaume and Wild, which avoids separation on the blade surface and reacts to the incoming flow by using a kinematic mechanism. In order to keep the complexity of such a slat device as simple as possible, the present research focuses on the development of a passive-adaptive slat which works without any actuation and electrical devices. The idea of this passive-adaptive slat device is based on the research of Petrikat²⁰ and Braun.²¹

The main objective of this research is to design a passive-adaptive slat for the airfoil DU-91-W2-250, which is a segment of the reference rotor blade in the project SmartBlades 2.0. It shall open passively with reference to the inflow for high angles of attack. When the slat is open, the stall angle of the airfoil shall be delayed to avoid separation and to increase the maximum lift of the airfoil. When the slat is closed, the lift to drag ratio shall be increased in comparison to the airfoil with an open slat for small angles of attack. In the following report, the design of the slat and its completely open position is described first. Afterwards, the design of two different mechanisms for opening and closing the slat passively is presented. The principle as well as the design of the passive-adaptive slat kinematics is presented for a scaled two-dimensional wind tunnel model, which will be investigated in upcoming measurements at ForWind, University of Oldenburg. Based on the developed passive-adaptive slat design, Section 4 discusses how such a passively movable slat can be integrated into a rotor blade of a full-scale wind turbine.

2 | DESIGN OF THE SLAT GEOMETRY

The first step to design the passive-adaptive slat kinematics is the design of the slat shape and the slat position when completely open. This is necessary because the slat kinematics and its passive-adaptive movement can only be designed when the aerodynamic behavior of the airfoil including the slat is known. The slat geometry was designed by the use of a numerical optimization procedure developed within the PYRANHA²² framework. PYRANHA offers different optimization algorithms to solve an extremum problem. The scheme of the optimization process is described in Figure 1.

In the beginning of the design process, a baseline geometry is defined, which shall be optimized (Figure 1, gray). In this case, the DU-91-W2-250 airfoil with an integrated slat¹⁶ was defined as baseline geometry and is outlined in Section 2.1. Afterwards, the design parameters

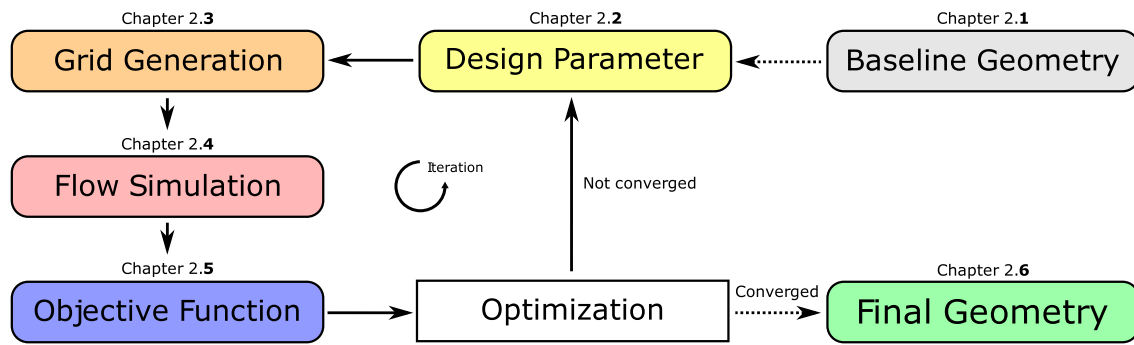


FIGURE 1 Scheme of the design process to optimize the shape and position of the passive-adaptive slat for a DU-91-W2-250 airfoil

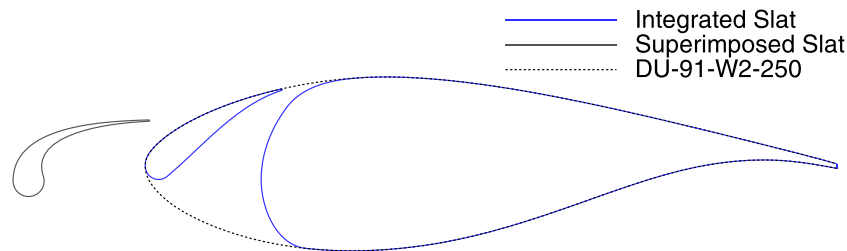


FIGURE 2 Manso Jaume and Wild's¹⁶ integrated slat design and superimposed slat design for the original DU-91-W2-250 profile

(yellow) for the slat's shape and position, which are changed during the optimization process, are presented in Section 2.2. For each new geometry, an analysis of its aerodynamic behavior has been performed. This consists of the generation of a new computational grid—described in Section 2.3—and a numerical analysis by Computational Fluid Dynamics (CFD), described in detail in Section 2.4. The main part of this optimization process is the solving of the extremum problem by minimizing the objective function (blue). The objective function is described in Section 2.5. The optimization procedure is performed in several iterations until an optimum of the objective function, and therefore, a final geometry is found. The final geometry (green) that is developed during the process is described in the end in Section 2.6.

2.1 | Baseline geometry

The baseline geometry of the present research article is based on the investigations made by Manso Jaume and Wild.¹⁶ They have designed an integrated rigid slat as well as a superimposed rigid slat for a DU-91-W2-250 airfoil (see Figure 2). Manso Jaume and Wild defined their integrated slat by dividing the original DU-91-W2-250 airfoil into a main profile and a slat. In contrast, the superimposed slat was placed in front of the original DU-91-W2-250 airfoil, which was used as main profile in this configuration.

Manso Jaume and Wild compared the aerodynamic performance of the designed integrated rigid slat to the aerodynamic performance of the designed superimposed rigid slat configuration. According to their research, the integrated slat leads to a higher maximum angle of attack of the airfoil than the superimposed slat and to a better aerodynamic performance in terms of the airfoil's efficiency. The passive-adaptive slat geometry is therefore based on the integrated rigid slat of the DU-91-W2-250 airfoil developed by Manso Jaume and Wild.

The first step of the passive-adaptive slat design was to generate a closed slat wing contour by extending the rigid integrated slat of Manso Jaume and Wild to the main airfoil. The resulting closed slat configuration is the baseline geometry of the passive-adaptive slat design process and can be seen in Figure 3 (bottom).

When looking at the baseline geometry of the closed passive-adaptive slat configuration, the open contour between the main airfoil and the slat's lower side is attracting attention. This design is chosen because according to Braun,²¹ an open wing contour at the lower side of the airfoil improves the opening movement of the passive-adaptive slat. This is due to the fact that a stagnation area between the closed slat and the main airfoil is developing, when the air is flowing around the airfoil (see Section 2.6). Hence, the region of the lower side of the slat has a higher static pressure than the region on the upper side of the slat. The slat thus tends to be pulled away from the main profile even at low flow velocities, which increases the tendency of the slat to open. Furthermore, the slat's lower side can be designed without the boundary condition that it needs to fit to the leading edge of the main airfoil, when the slat is closed, which increases the design space of the slat contour. Additionally, the main

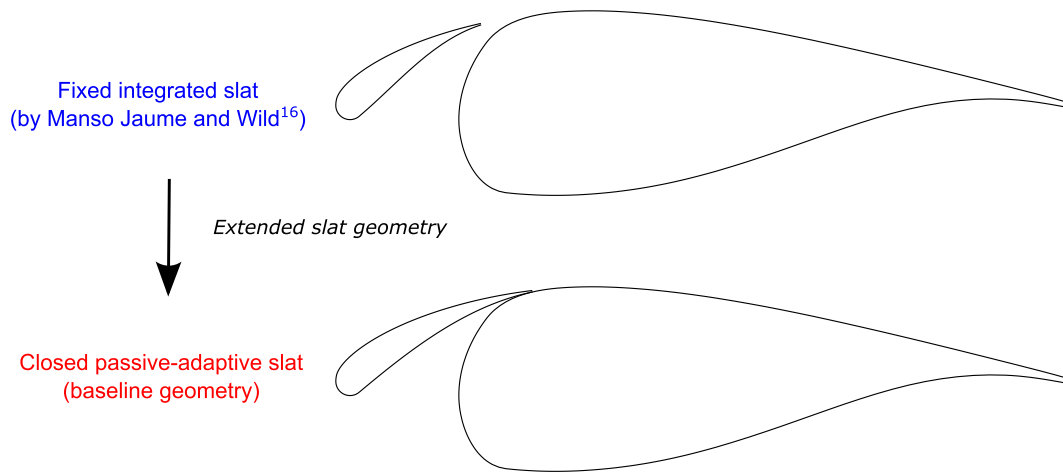


FIGURE 3 Geometry of the DU-91-W2-250 airfoil with fixed integrated slat (top)¹⁶ and with integrated slat with increased chord length as baseline geometry for the DU-91-W2-250 airfoil with closed passive-adaptive slat (bottom)

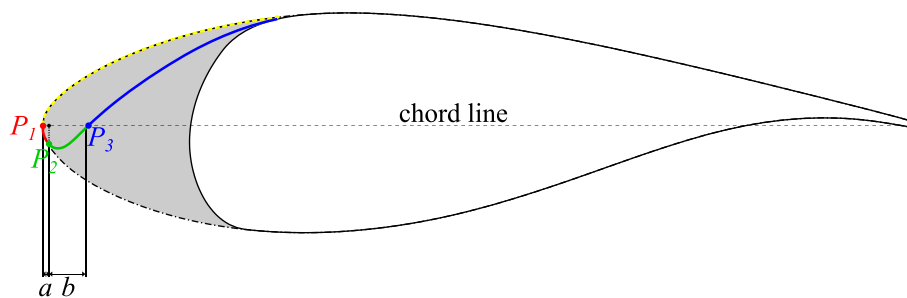


FIGURE 4 Baseline geometry of the DU-91-W2-250 profile with integrated slat and optimization parameters of the slat shape “*a*” and “*b*”

airfoil shape has a high curvature in the region where the slat trailing edge is positioned, which has a positive effect on the slats dumping effect according to Smith.¹²

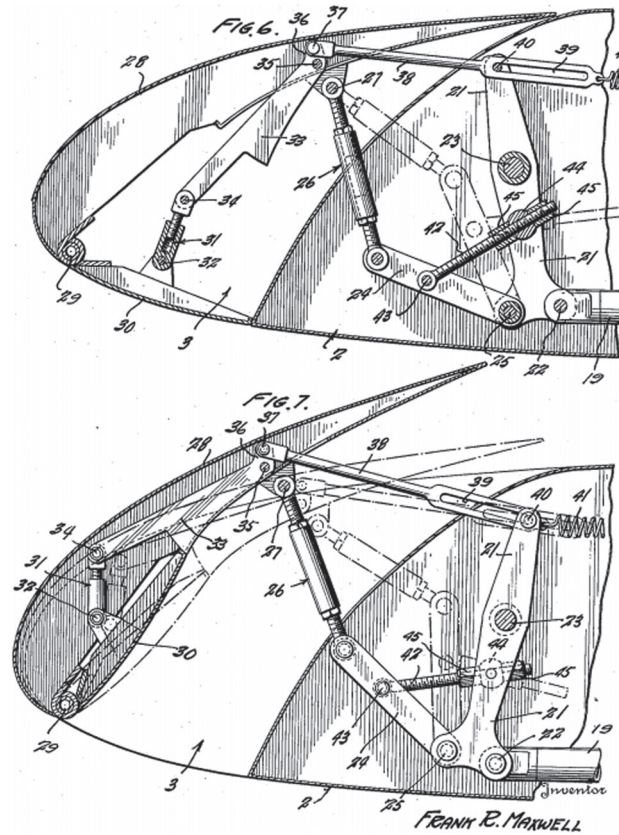
2.2 | Design parameter

In the beginning of the slat shape optimization, different design strategies were tested. With reference to the lift and drag of the airfoil, the most promising design was reached by describing the two-dimensional slat contour with four separate splines with tangentially constant transition. Since the slat is designed as integrated geometry, one boundary condition for the suction side of the slat is given by the shape of the DU-91-W2-250 airfoils upper side. The yellow spline in Figure 4 is therefore following the contour of the DU-91-W2-250 airfoils upper side until point P_1 , which is equal to the leading edge of the original airfoil. The red spline keeps on following the contour of the DU-91-W2-250 airfoil until point P_2 , which is defined by the distance a . The green spline is connecting point P_2 with point P_3 on the chord line defined by parameter b . The blue spline is connecting point P_3 and the slat trailing edge. The minimal thickness of the slat trailing edge (t_{TE}) is defined in relation to the airfoil chord length (c) as $t_{TE}/c = 0.002$ to guarantee the mechanical strength of a model during upcoming wind tunnel investigations. The bounds of the design parameters a and b (see Table 1) are given by the contour of the original DU-91-W2-250 airfoil and the leading edge region of the main airfoil. The resulting design space of the slat shape is represented by the gray area in Figure 4.

The open slat position is defined by rotating the closed slat around a virtual hinge S_{rot} . In addition to the slat shape, the coordinates of this slat rotation point S_{rot} as well as the gap size between the trailing edge of the open slat and the main airfoil are subject to changes during the optimization process. The bounds of the x and y -coordinates of the slat rotation point were defined as $0 < S_{rot,x}/c < 0.5$ and $0.05 < S_{rot,y}/c < 2.0$ with reference to the leading edge of the original DU-91-W2-250 airfoil. The baseline position of the slat rotation point was defined below the chord line close to the lower front region of the main airfoil to avoid a great slope of the extension curve of the slat trailing edge. For a better understanding, a slat design by Maxwell²³ is shown in Figure 5. In this slat design, the slat opens with the slat leading edge high above the main airfoil. Braun²¹ observed in his studies of the aerodynamic impact of the slat movement that an extension of the slat with such a high slope can lead to

TABLE 1 Design parameters of the slat shape and the open slat position including the parameter bounds during the optimization

$a/c [-]$	$b/c [-]$	$gap/c [-]$	$S_{rot,x}/c [-]$	$S_{rot,y}/c [-]$
0.01–0.06	0.00–0.06	0.01–0.026	0.00–0.50	0.05–2.00

**FIGURE 5** Slat design of Maxwell23 with the slat trailing edge extended high above the main airfoil

detachment phenomena at the slat trailing edge. Such an opening behavior was noticed in the preliminary studies of the passive-adaptive slat design, too, which explains why the baseline and the bounds of the design parameters were chosen as mentioned.

The geometry of the open and closed slat including the three parameters, which are defining the open slat position, can be seen in Figure 6. The design parameters are varied during the optimization process, and a new flow simulation was carried out for each resulting geometry.

2.3 | Grid generation

For every evaluated airfoil geometry, two block structured grids were generated by using the DLR grid generation tool MegaCADs.²⁴ The grid for the airfoil with closed slat consists of about 73k points and the grid for the completely open slat geometry consists of about 98k points. Both geometries are meshed in a two-dimensional grid, which is designed as C-type grid for three multigrid levels. The resolution of the boundary layer is obtained by at least 32 cells in the region normal to the wall and a first wall spacing that achieves a y^+ value of about 1. The block topology and the grid resolution are following best practices obtained from mesh sensitivity studies for high-lift system flows.²⁵ The nearfield of the two different grids is shown in Figure 7 for both configurations.

2.4 | Flow simulation

The investigated DU-91-W2-250 airfoil is a section profile of the reference rotor blade in the project SmartBlades.²⁶ Hence, the inflow conditions for the optimization of the slat geometry are the flow conditions at the airfoils section for the blades design tip-speed-ratio. The inflow boundary conditions, which were used in every simulation presented in this article, are shown in Table 2.

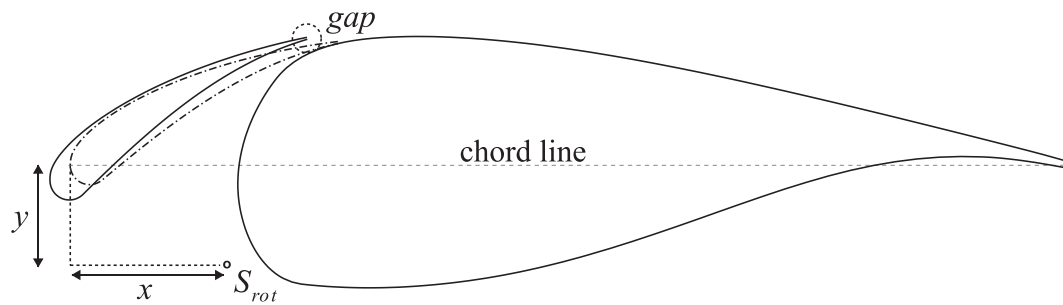


FIGURE 6 Baseline geometry of the DU-91-W2-250 profile with integrated slat and optimization parameters of the slat opening (rotation point coordinates “ $S_{rot,x}$ ”/“ $S_{rot,y}$ ” and gap width “ gap ”)

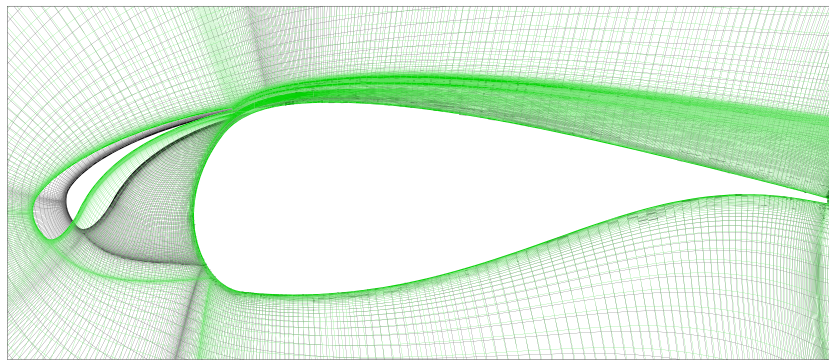


FIGURE 7 Grid of the DU-91-W2-250 airfoil with integrated slat generated with MegaCADs for the closed (black) and open slat configuration (green)

TABLE 2 Inflow conditions at the profile of the investigated rotor blade at design tip-speed-ratio

Airfoil	Mach number [–]	Reynolds number [10^6]
DU-91-W2-250	0.1077	7.89

The simulations were performed with Reynolds-Averaged-Navier–Stokes calculations using the Spalart–Allmaras one-equation turbulence model. The used flow solver is the DLR FLOWer code,²⁷ which is a block structured code based on a finite-volume formulation. The simulations in this study were run considering steady-state flow conditions. For steady calculations, the DLR FLOWer code offers the use of residual smoothing and several multigrid methods. In every simulation presented in this article, the inflow was defined as uniform at the farfield boundary, and the surface's boundary layer was set to fully turbulent. The DU-91-W2-250 airfoil has already been investigated in several researches using a condition of a fully turbulent boundary layer.^{28–30} Within flow simulations and at scaled wind tunnel models, the position of the laminar-turbulent transition is usually fixed to simulate a contamination of the leading edge, which appears at full-scale rotor blades. Furthermore, a laminar separation bubble can occur on small wind tunnel models with a clean surface and a low Reynolds number flow, which deteriorates the aerodynamic performance of the airfoil.³¹ In these cases, the position of the laminar-turbulent transition is fixed by tripping the leading edge of the airfoil. Sensitivity studies by Timmer and van Rooij^{28,29} have shown that the maximum lift coefficient of wind turbine profiles like the DU-91-W2-250 is significantly reduced, when the leading edge is tripped to generate a fully turbulent boundary layer. In their studies, they placed a 0.35-mm-thick zigzag tape on the top surface of the DU-91-W2-250 airfoil at $x/c = 0.05$ and compared the aerodynamic performance of the airfoil with the aerodynamic performance of the DU-91-W2-250 in clean configuration at a Reynolds number of $Re_{\infty, Timmer} \approx 3e6$. Their studies have shown that the maximum lift coefficient decreases by up to 15% when the leading edge is tripped. Accordingly, the aerodynamic performance of the original DU-91-W2-250 airfoil is much higher with the use of laminar-turbulent transition instead of a condition of a fully turbulent boundary layer. Comparable results were found out in the investigations of Manso Jaume et al.³² during investigations of the DU-91-W2-250 airfoil with a slat device. Manso Jaume et al. investigated the DU-91-W2-250 airfoil including the superimposed slat (see Section 2.1) with the help of wind tunnel measurements at ForWind, University of Oldenburg, at a Reynolds number of about $Re_{\infty, MansoJaume} \approx 0.6e6$ both with and without tripping. They have found out that the maximum lift coefficient of the configuration with tripped superimposed slat is decreased about 11% compared to the maximum lift coefficient of the non-tripped configuration. Manso Jaume et al. also found out during the wind tunnel measurements without tripping

that the described laminar bubble developed at the leading edge of the superimposed slat. Because of the laminar separation bubble, the lift curve was suddenly breaking, and the drag increased significantly once it completely separated. As mentioned before, such a laminar bubble occurs at scaled wind tunnel models due to the low Reynolds number flow. For this reason, the upcoming investigations on the wind tunnel model of the DU-91-W2-250 airfoil are carried out with a tripped slat leading edge, and the surface's boundary layer is set to fully turbulent in the simulations of the present study. As described, the tripped leading edge especially influences the near stall region including the maximum lift coefficient of the investigated airfoils. However, the range of application of the passive-adaptive slat kinematics is mainly designed for smaller angles of attack (see Section 3), which means that the functioning is not particularly affected by the condition of a fully turbulent boundary layer. The presented design is therefore also likely to be very robust against leading edge contamination, but this remains to be shown in further studies.

Manso Jaume et al. have shown as well that the numerical simulations with the use of a fully turbulent boundary layer condition were in great accordance in comparison to the wind tunnel tests with tripping. Wild²⁵ pointed out as well that the DLR FLOWer code predicts the aerodynamic coefficients of lift and drag even in the near stall region very precisely in comparison to wind tunnel tests of airfoils with a slat device. Hence, the DLR FLOWer code is fast, robust, and accurate, which makes it a good choice as simulation tool especially for the high-lift design of the passive-adaptive slat.

2.5 | Objective function

The objective function summarizes the aerodynamic performance of the airfoil for the closed as well as the open slat configuration in a single value. Since an aerodynamically well-designed airfoil should have a low drag and a high lift, the glide ratio c_L/c_D is a typical choice for a formulation of an objective function. c_L and c_D are the sectional lift and the drag coefficient, respectively. To investigate whether the glide ratio is a suitable part of the final objective function for the slat design, numerical simulations of the flow around the baseline geometry with open and closed slat were carried out first. The resulting force polar of the baseline geometry is presented in Figure 8 in comparison to the iso-lines of the objective functions $F_{obj,1} = -c_L/c_D$ (glide ratio, left) and $F_{obj,2} = -c_L^3/c_D^2$ (squared climb index, right). The results are presented for the closed slat configuration until $\alpha_{max,closed} = 13^\circ$ and for the open slat configuration until $\alpha_{max,open} = 31^\circ$. In both cases, a complete stall occurs on the main airfoil for higher angles of attack, which is a highly unsteady flow phenomena and cannot be predicted with sufficient accuracy by steady-state flow simulations.

Along the iso-lines, the two different objective functions have a constant value. The iso-lines of the glide ratio are straight lines that intersect with the polars of the baseline geometry with closed and open slat. In contrast to the glide ratio, the iso-lines of the squared climb index are more aligned to the polars, especially in the medium range of the drag and lift coefficients where an optimization is beneficial. Accordingly, changes of $F_{obj,2} = -c_L^3/c_D^2$ are in this region not as sensitive to variations of boundary conditions such as the angle of attack. Hence, the use of the squared climb index in the final objective function instead of the glide ratio enables a robust slat design independent of the exact choice of the inflow conditions especially in the region where an aerodynamic optimization is advantageous.

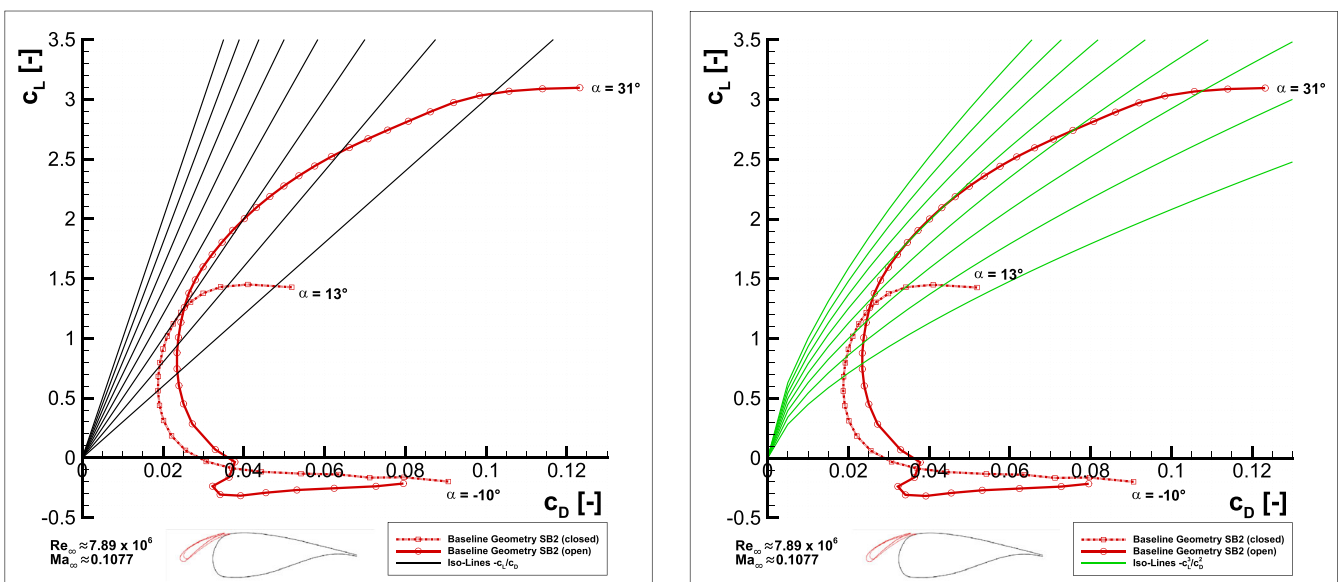


FIGURE 8 Lift coefficient over drag coefficient of the baseline geometry with open and closed passive-adaptive slat including the iso-lines of the objective functions $F_{obj,1} = -c_L/c_D$ (glide ratio, left) and $F_{obj,2} = -c_L^3/c_D^2$ (squared climb index, right)

For the development of the final objective function, it was afterwards determined at which angle of attack the slat should open to define the operational range for the closed and open slat configuration. The aerodynamic behavior of the baseline geometry was therefore investigated by the use of the lift coefficient and the mentioned squared climb index (see Figure 9).

In Figure 9 (left), it can be seen that the lift coefficient of the baseline geometry is greater with open slat than with closed slat for $\alpha > 7^\circ$. Since $\alpha = 7^\circ$ is a little smaller than the angle of attack of the maximum lift coefficient of the baseline geometry with closed slat ($\alpha_{c_{L,max,closed}} = 12^\circ$) and the closed slat configuration has a higher lift to drag ratio than the open slat configuration for $\alpha < 7^\circ$, the opening angle of attack for the passive-adaptive kinematics 1 was defined as $\alpha_{open,Kin1} = 7^\circ$. Since $\alpha_{open,Kin1} = 7^\circ$ is the maximum angle at which the slat is still retracted, the closed slat geometry was optimized for this angle. In order to take into account both the lift and the drag of the geometry, the optimization was carried out with reference to the mentioned squared climb index.

The open slat position was optimized for the angle of attack of the maximum climb index of the baseline geometry with open slat, which is at $\alpha = 14^\circ$ according to Figure 9 (right). Furthermore, preliminary studies for the slat shape and position design have shown that it is also necessary to include an angle of attack close to the angle of attack of $c_{L,max}$ of the open slat configuration in the objective function to make sure that the stall angle of attack of the airfoil is not decreasing during the optimization process. For this reason, the lift coefficient at $\alpha = 30^\circ$ for the airfoil with open slat is additionally included in the objective function. There may be a reduced reliability in predicting the aerodynamic behavior of the airfoil with the passive-adaptive slat in the near stall region using steady-state flow simulations for the exact prediction of the stall onset and corresponding lift values. On the contrary, the inclusion of an angle of attack close to the angle of attack of $c_{L,max}$ is in this case mainly used to avoid a reduction of the maximum angle of attack. But as this is a comparative value within the same simulation environment, a reduced predicted angle will largely reduce the corresponding lift coefficient and direct the optimization away from such a risk. For the correct operation of the passive-adaptive slat, an accurate prediction of its aerodynamic behavior by numerical flow simulations is more crucial for smaller angles of attack, especially where the slat opens and closes. Furthermore, as mentioned in Section 2.4, the DLR FLOWer code predicts the near stall behavior of an airfoil with a slat device even in steady-state simulations very well in comparison to wind tunnel tests.

Overall, the objective function F_{obj} is defined as follows:

$$F_{obj}(\vec{x}) = - \sum_{i=1,2,3} w_i * F_i(\vec{x}) \quad (2.1)$$

$$F_1(\vec{x}) = \left[\frac{c_L^3}{c_D^2} \right]_{closed,\alpha=7^\circ} / \left[\frac{c_L^3}{c_D^2} \right]_{closed,\alpha=7^\circ, ref} \quad (2.2)$$

$$F_2(\vec{x}) = \left[\frac{c_L^3}{c_D^2} \right]_{open,\alpha=14^\circ} / \left[\frac{c_L^3}{c_D^2} \right]_{open,\alpha=14^\circ, ref} \quad (2.3)$$

$$F_3(\vec{x}) = [c_L]_{open,\alpha=30^\circ} / [c_L]_{open,\alpha=30^\circ, ref} \quad (2.4)$$

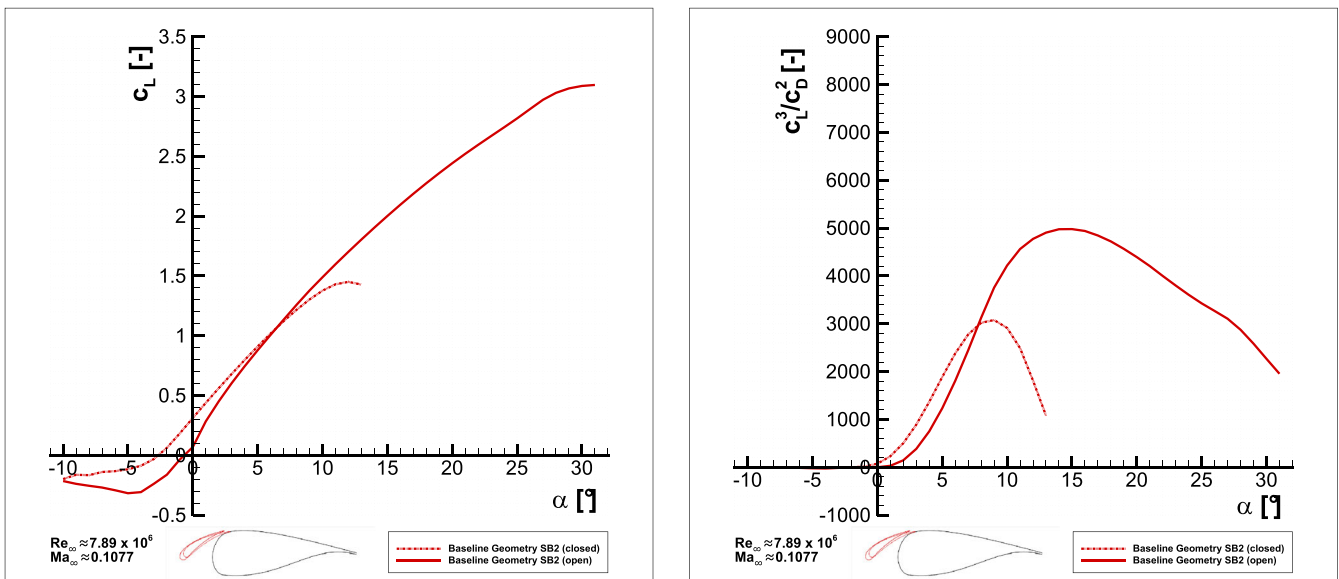


FIGURE 9 Lift coefficient (left) and squared climb index (right) of the DU-91-W2-250 airfoil with the baseline of the passive-adaptive slat

The squared climb index c_L^2/c_D^2 for the open and closed slat as well as the lift coefficient c_L for $\alpha = 30$ were weighted by the factors w_i with $w_1 = 0.3$, $w_2 = 0.3$, and $w_3 = 0.4$. For each of the three cases F_i that are considered in the objective function F_{obj} , a flow simulation was carried out. Afterwards, the aerodynamic coefficients of the geometry were calculated and used for the objective function.

2.6 | Results of the optimization process

The final geometry was determined by using the SUBPLEX algorithm to find a minimum of the objective function by varying the design parameters step by step. The SUBPLEX algorithm is a gradient-free optimizer developed by Rowan.³³ The algorithm has a good convergence rate because it solves extremum problems by separating the optimization in several low-dimensional subspaces. In these subspaces, the Simplex method is used to find a solution for the optimization problem, which is very efficient in low-dimensional cases. Wild²⁵ has shown that the SUBPLEX algorithm is suitable for the design of high-lift systems. Therefore, the SUBPLEX algorithm is chosen to optimize the integrated slat geometry in an efficient way. The final geometry, which was detected by the optimization procedure, is compared to the baseline geometry in Figure 10.

The comparison of the baseline geometry with the optimized geometry shows that the camber of the optimized slat is increased significantly. Moreover, the final open slat position is further upstream in comparison to the position of the open slat in the baseline geometry, which results in an increased total chord of the optimized geometry. In addition, the overlap of the optimized open slat and the main airfoil is reduced, and the position of the trailing edge of the optimized open slat is changed closer towards the point of strongest curvature of the main airfoils upper side. The position of the trailing edge is hereby close to the region of minimum pressure of the main airfoil during flow stream, which has a positive effect on the slats dumping effect according to Smith.¹² In Figure 11, the final geometry with closed and open slat is compared to the fixed integrated slat and the original DU-91-W2-250 airfoil. As mentioned before, the chord length and the camber of the optimized slat (Figure 11, green) are significantly increased in comparison to the original fixed integrated slat (Figure 11, blue).

To analyze the aerodynamic behavior of the optimized geometry in comparison to the baseline geometry, the lift curve and the squared climb index are shown in Figure 12. Hereby, the significant increase in the squared climb index by up to 10% and by round about 5% in the maximum lift of the optimized airfoil geometry with open slat compared to the baseline geometry have to be mentioned. The increase in lift can be explained by the increased camber of the optimized slat, which contributes a higher lift by itself, and by the increased overall chord length of the optimized airfoil in comparison to the baseline geometry. The increased chord length of the optimized airfoil also explains the increased slope of the lift curve compared to the lift curve of the baseline geometry. Furthermore, the comparison of the lift curves of the closed and the open final geometry shows clearly that the lift coefficients in the region of the slats opening ($\alpha_{open, kin1} = 7^\circ$) only slightly differ between these two configurations. This transition between the two lift curves allows a smooth movement of the slat.

In Figure 13, the lift and the drag coefficients as well as the squared climb index of the optimized airfoil, the original DU-91-W2-250 airfoil, and the airfoil with fixed integrated slat by Manso Jaume and Wild¹⁶ are compared to each other. First of all, the increase in the maximum lift coefficient (Figure 13, top-left) and in the maximum climb index (Figure 13, bottom) of the optimized geometry with moveable passive-adaptive slat in comparison to the airfoil with fixed integrated slat have to be mentioned. The increase in lift is mainly the result of three changes: The optimized slat geometry has a significantly larger chord length than the geometry developed by Manso Jaume and Wild, which results in a changed

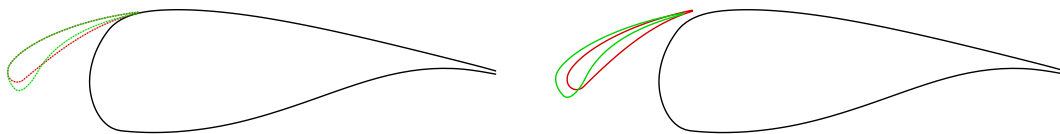


FIGURE 10 Final geometry (green) of the passive-adaptive slat for the DU-91-W2-250 airfoil in closed (left) and open (right) configuration in comparison to the baseline geometry (red)

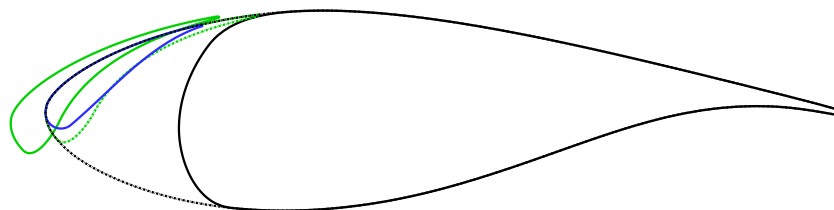


FIGURE 11 Final geometry with passive-adaptive slat in open (green) and closed (green dotted) configuration in comparison to the geometry with fixed integrated slat (blue) and the original DU-91-W2-250 airfoil (black dotted)

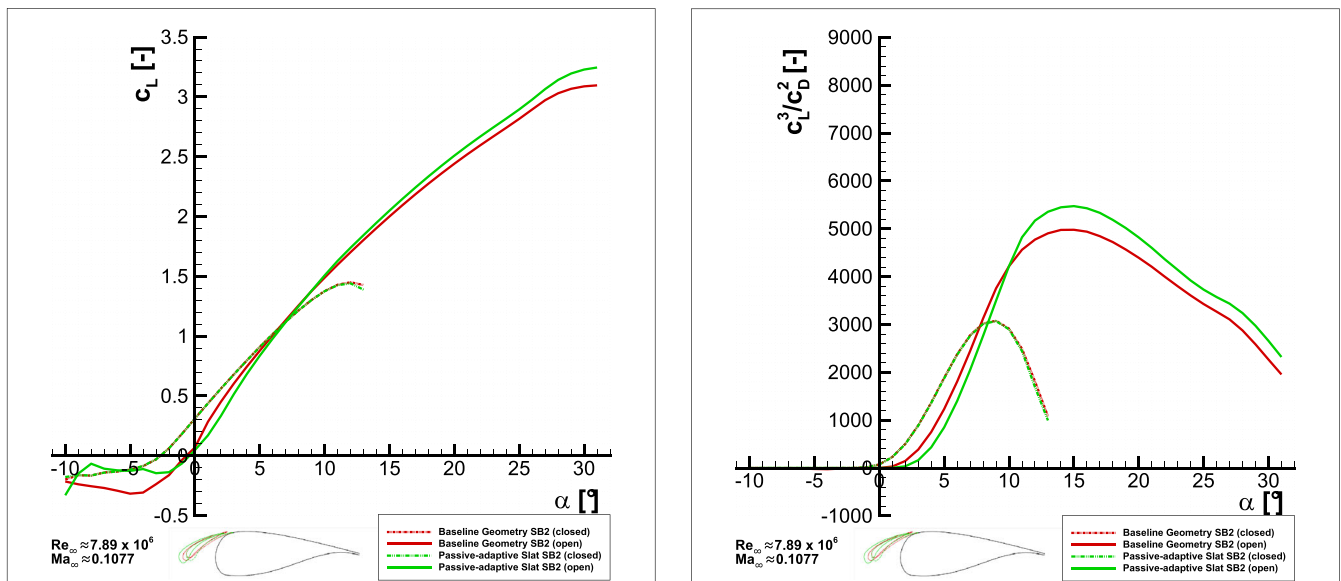


FIGURE 12 Lift coefficient (left) and squared climb index (right) of the DU-91-W2-250 airfoil with optimized passive-adaptive slat and the baseline geometry

slope in the lift curve. In addition, the optimized slat has a higher camber than the fixed integrated slat. The increased circulation around such a larger and more cambered slat increases the slat effect, which causes a reduction of the suction peak on the main profile and therefore a delay in the tendency of the airfoil flow to separate.¹² This results in a stall delay with the optimized slat geometry. The slightly closer gap supports this effect additionally. All these geometry changes result in an increased lift coefficient of the optimized open geometry compared to the original geometry for $\alpha > 8^\circ$. Further, the configuration with closed passive-adaptive slat shows a smaller drag coefficient and a higher lift coefficient than the airfoil with fixed integrated slat for $\alpha < 7^\circ$. The moveable passive-adaptive slat has therefore significant advantages compared to the fixed integrated slat.

The positive effect of the designed geometry is the typical slat behavior, which can be seen in Figure 13 (top-left). The $c_{L, max}$ of the final geometry including the optimized slat has an increase by almost 130% due to a 20° increase in the angle of attack of $c_{L, max}$ in comparison to the original DU-91-W2-250 airfoil. Also, the maximum climb index of the final geometry is increased by about 20% in comparison to the original airfoil (Figure 13, bottom).

When the slat position is closed, however, the climb index is significantly lower than the climb index of the original airfoil. This is especially a result of a higher drag of the final geometry for angles of attacks less than 10° (Figure 13, top-right). The increased total drag of the airfoils with slat in comparison to the original airfoil is caused by the lower side cavity due to the slat integration. The airfoil's drag is reduced by the optimization and the use of a moveable passive-adaptive slat instead of a fixed slat though, but nevertheless, further investigations of an airfoil with integrated passive-adaptive slat and a low total drag at the same time needs to be done.

However, the advantage of a stall delay can be seen in the drag coefficient as well: For $\alpha > 11^\circ$, a significant increase in drag can be seen for the DU-91-W2-250 airfoil without a slat. This drag increase is caused by a separation on the DU-91-W2-250, whereas the flow on the main airfoil of the geometry with passive-adaptive slat is still attached.

In summary, the DU-91-W2-250 airfoil with closed passive-adaptive slat achieves a comparable $c_{L, max}$ and a slightly higher angle of attack of $c_{L, max}$ but also has the disadvantage of a slightly higher drag coefficient compared to the original DU-91-W2-250 airfoil. At the same time, the airfoil's $c_{L, max}$ and the angle of attack of $c_{L, max}$ are greatly increased when the passive-adaptive slat is open. The passive-adaptive slat is meant to be integrated in the root region of a wind turbine's rotor blade, which primarily operates at high local angles of attack. Daniele et al. and Teßmer et al.^{34,35} have shown with the use of CFD and BEM simulations that the local angle of attack is greater than 10° in the root region ($0.0 < r/R_{Blade} < 0.25$) of the reference rotor blade from the project SmartBlades at the rated wind velocity. Hereby, the root region of the reference rotor blade operates with a partially detached flow on the upper blade surface,³⁶ which can be avoided with the help of an open passive-adaptive slat. The advantage of the passive-adaptive slat at high angles of attack accordingly outweighs the disadvantage at smaller angles of attack. In addition, the passive-adaptive slat can adapt to a gusty inflow and thus improve the aerodynamic performance of the blade segment on the one hand and presumably also contribute to load reduction on the other hand. However, this has to be investigated further in subsequent studies.

For a further comparison of the aerodynamic improvement due to the passive-adaptive slat, the studies by Hansen et al.³⁷ can be consulted. They designed aerodynamically shaped VGs and investigated their stall delay effect in comparison to typical thin plate VGs in wind tunnel tests

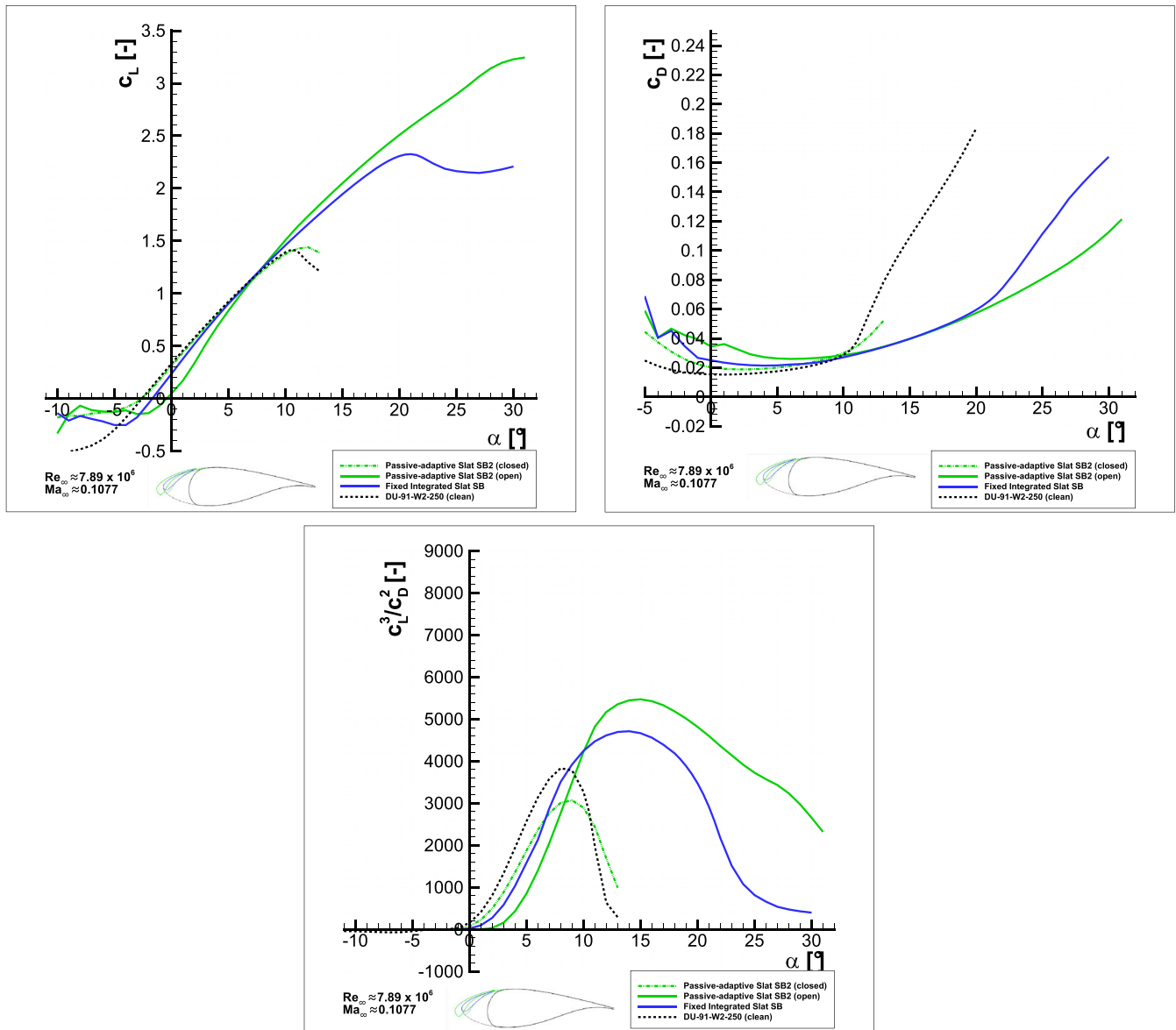


FIGURE 13 Lift coefficient (top-left), drag coefficient (top-right), and squared climb index (bottom) of the optimized geometry with passive-adaptive slat, the airfoil with fixed integrated slat, and the original DU-91-W2-250 airfoil

with the DU-91-W2-250 airfoil. Their wind tunnel investigations were made with nearly the same Reynolds number ($Re_{\infty, \text{Hansen}} \approx 6.1e6$) as presented in this research article. Overmore, the measurement of Hansen et al. with the clean profile DU-91-W2-250 showed nearly the same maximum lift coefficient ($c_{L, \text{max}} = 1.44$) at nearly the same angle of attack ($\alpha_{c_{L, \text{max}}} = 10.38^\circ$) as those obtained with the CFD simulations using the DLR FLOWER code (see Figure 13, top-left). The data of Hansen et al. can therefore be used for a first plausible classification of the results. In contrast to the airfoil with the designed passive-adaptive slat, only a stall incidence increase of round about 3° and a maximum lift coefficient of $c_{L, \text{max}} = 1.91$ could be reached with the VGs. When classifying the stall delay of round about 20° , which is reached with the use of the passive-adaptive slat, it must be said that such a value is a significant improvement in comparison to other state-of-the-art flow devices.

The influence of the slat on the flow around the main airfoil can also be seen in the pressure coefficient c_p . In Figures 14–16, the pressure coefficient of the DU-91-W2-250 with optimized passive-adaptive slat is presented in comparison to the pressure coefficient of the geometry with fixed integrated slat¹⁶ and the original DU-91-W2-250 airfoil for different angles of attacks.

In Figure 14, the pressure coefficients of the geometries for $\alpha = 0^\circ$ and $\alpha = 7^\circ$ are nearly the same. The main difference is caused by the gap between the slat and the main airfoil for the fixed integrated slat and due to the lower side cavity for both slat variants.

By comparing the pressure coefficient of the airfoils with slat at higher angles of attack in Figures 15 and 16 (left), it can be noticed that the suction peak on the fixed integrated slat and the passive-adaptive slat are almost identical. The main difference in the pressure coefficient of the

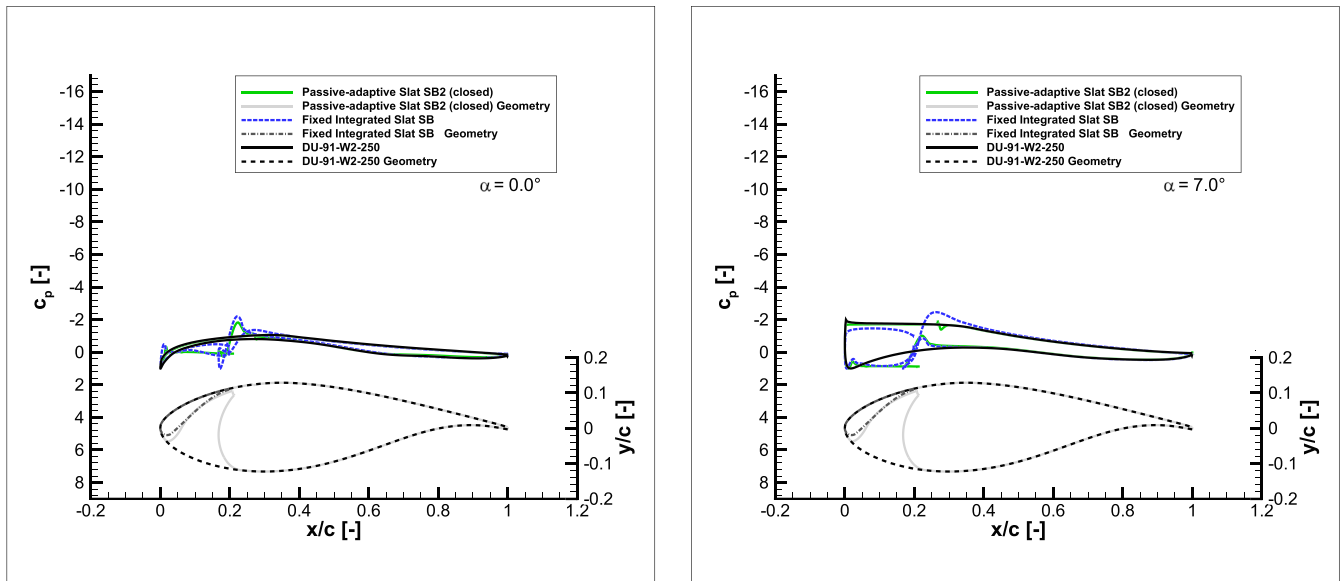


FIGURE 14 Pressure coefficient c_p of the original DU-91-W2-250 airfoil in comparison to the airfoil with fixed integrated slat and the airfoil with passive-adaptive slat for the closed configuration at $\alpha = 0^\circ$ (left) and at $\alpha = 7^\circ$ (right)

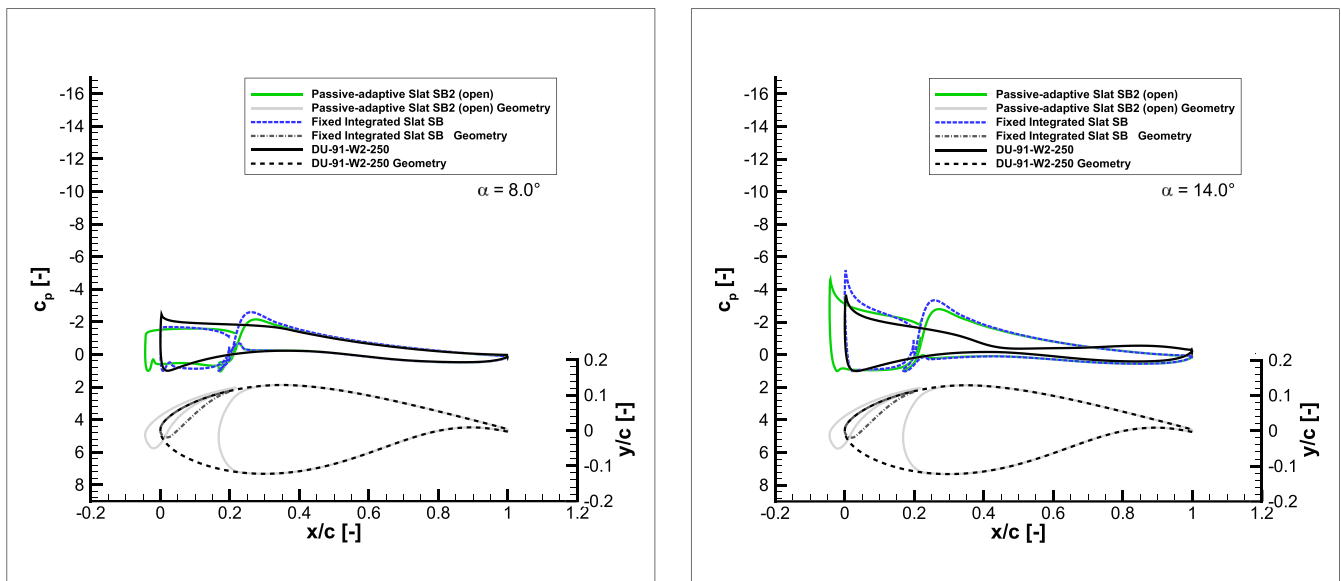


FIGURE 15 Pressure coefficient c_p of the original DU-91-W2-250 airfoil in comparison to the airfoil with fixed integrated slat and the airfoil with passive-adaptive slat for the open configuration at $\alpha = 8^\circ$ (left) and at $\alpha = 14^\circ$ (right)

slats is that the suction peak of the passive-adaptive slat, however, is further forward due to its lateral displacement. The main reason for the increase in lift on the passive-adaptive slat is accordingly the increase in the chord length. In Figures 15 and 16 (left), the reduced suction peak at the main airfoil with the passive-adaptive slat in comparison to the main airfoil with fixed integrated slat can be seen as well. As mentioned before, this is caused by the increased slat effect, due to greater circulation at the passive-adaptive slat compared to the fixed integrated slat. The reduced suction peak on the main airfoil leads to a stall delay, which can be seen especially in the pressure distribution at $\alpha = 28^\circ$, shown in Figure 16 (right). The pressure coefficient is constant on the suction side of the fixed integrated slat configuration for $x/c > 0.6$, which is caused by a separation on the main airfoil, whereas the pressure coefficient on the suction side of the main airfoil with passive-adaptive slat continues to decrease in this area as the flow is still attached.

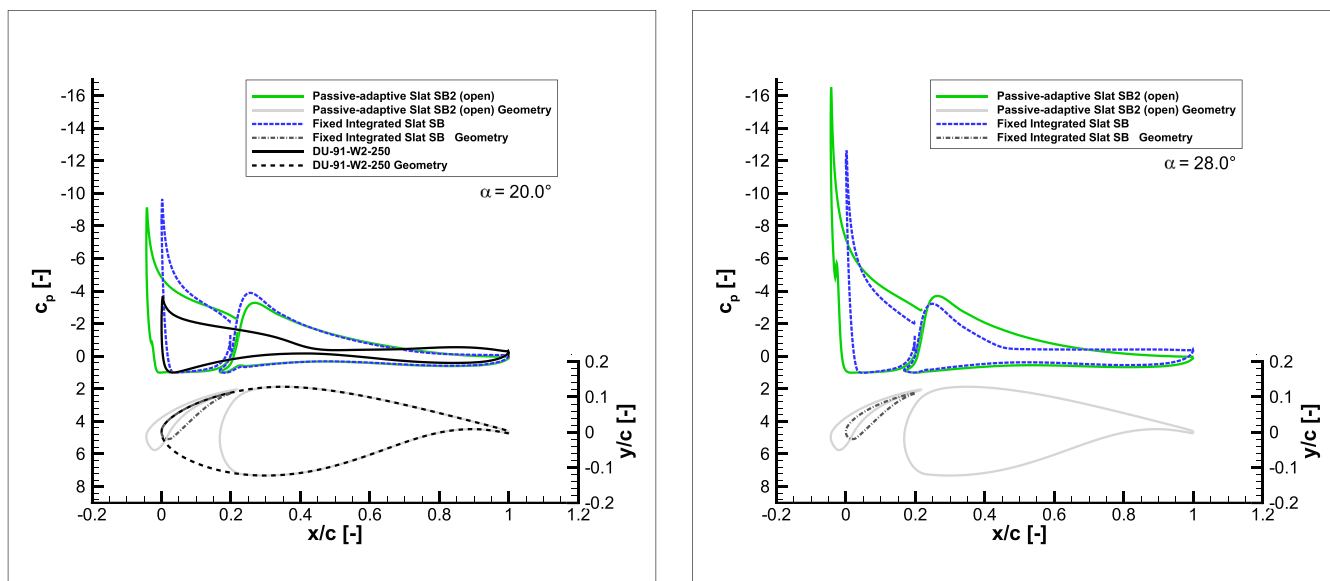


FIGURE 16 Pressure coefficient c_p of the DU-91-W2-250 airfoil with passive-adaptive slat in comparison to the airfoil with fixed integrated slat and the original airfoil at $\alpha = 20^\circ$ (left) and in comparison to the airfoil with fixed integrated slat at $\alpha = 28^\circ$ (right)

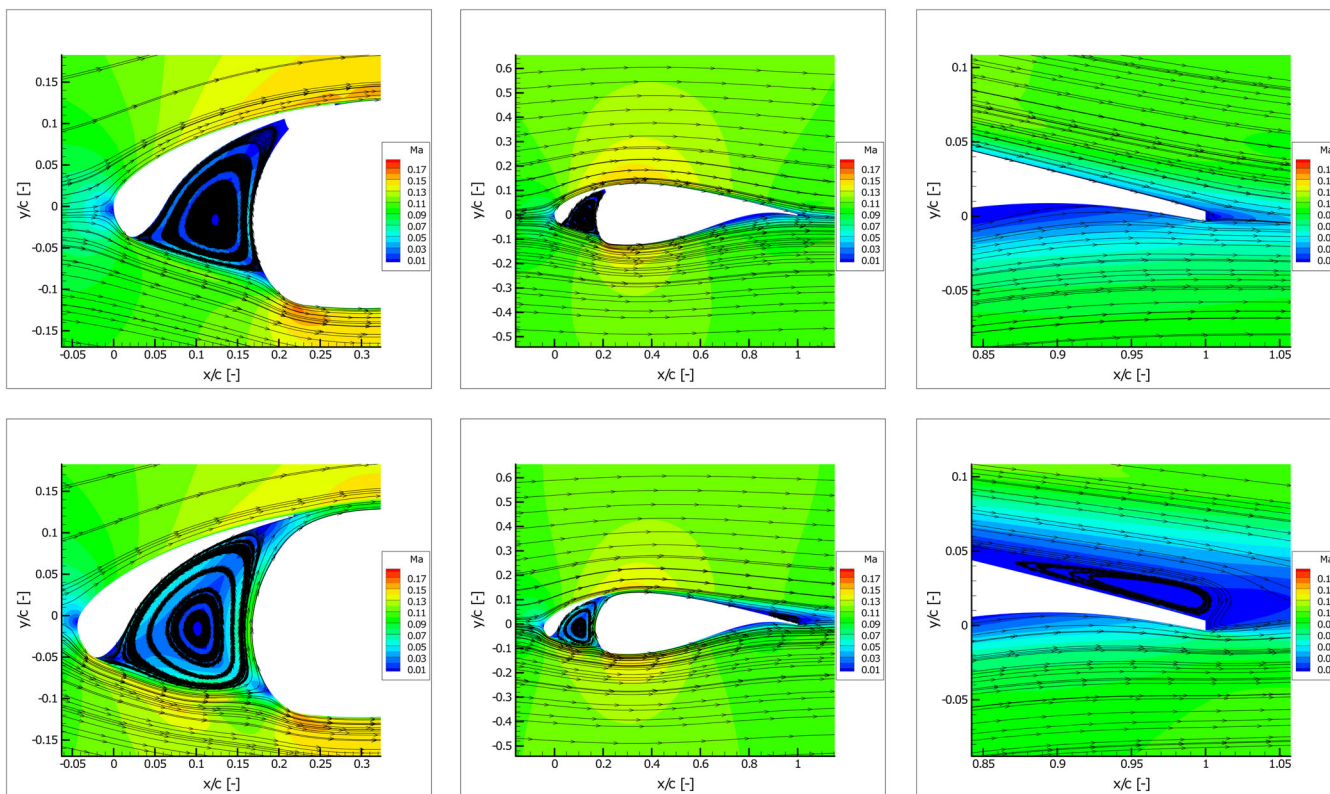


FIGURE 17 Flow field around the airfoil with optimized passive-adaptive slat for $\alpha = 0^\circ$ in closed (top) and open (bottom) configuration

For a better understanding of the flow phenomena that occur when using the passive-adaptive slat, the flow field around the closed as well as the open slat configuration is presented in Figures 17 and 18. First of all, the developed stagnation area between the slat and the main airfoil for the case with $\alpha = 0^\circ$ (Figure 17) has to be mentioned. When the slat is completely closed, the developed vortex extends throughout the whole lower side cavity of the airfoil. Such a flow phenomenon can be described as a trapped vortex,^{38,39} which is held stable in this body near position.

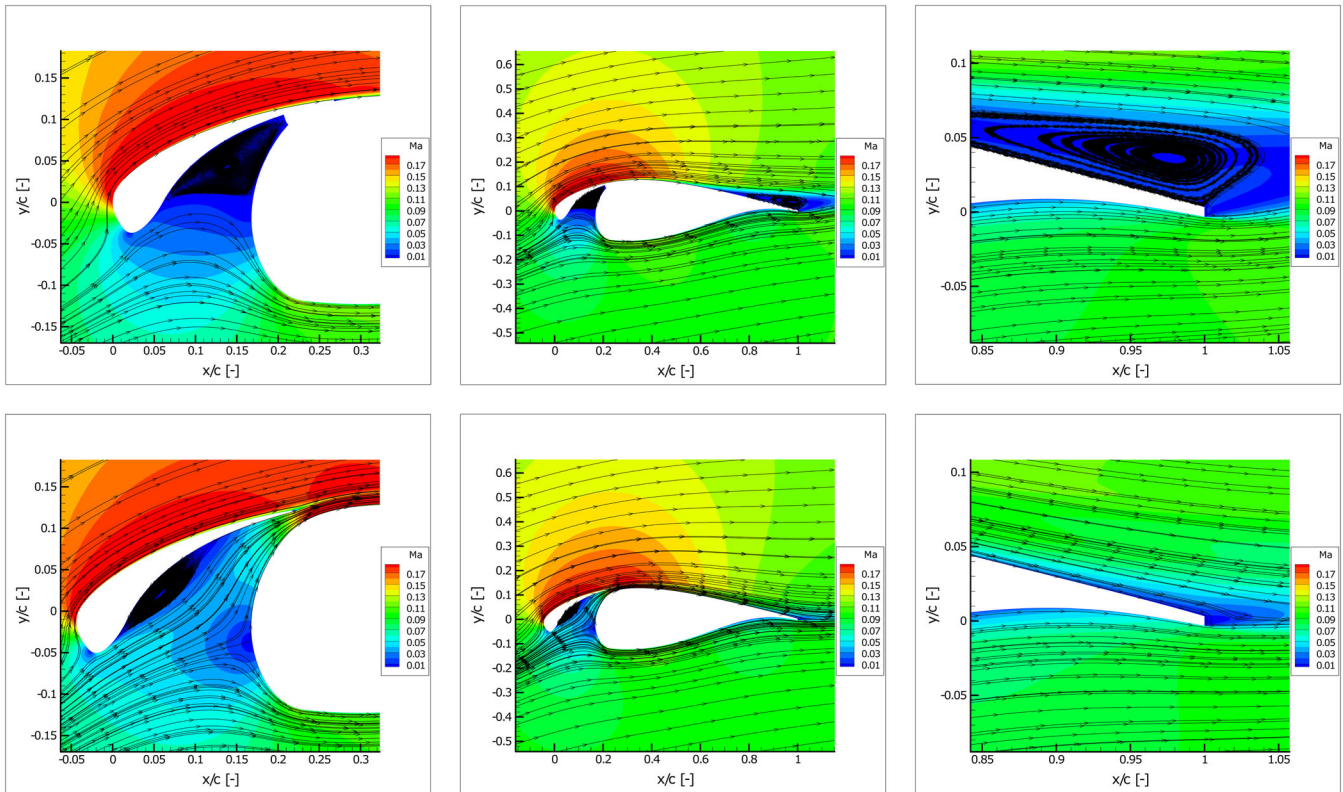


FIGURE 18 Flow field around the airfoil with optimized passive-adaptive slat for $\alpha = 12^\circ$ in closed (top) and open (bottom) configuration

The vortex enlarges the effective airfoil contour as sensed by the major passing flow. When looking at the flow on the upper side of the profile, however, no conspicuous flow phenomena can be observed in the closed configuration. The flow on the main airfoil is attached, which is similar to the behavior of the original DU-91-W2-250 airfoil in the clean configuration at low angles of attack. When the slat is open, the pronounced recirculation area at the lower side of the slat occurs as well. Because of the extended vortex, there is hardly any gap flow, which has a negative impact on the boundary layer of the main airfoil resulting in a separated flow at the trailing edge region for $x/c > 0.7$.

In Figure 18, a flow separation for $x/c > 0.6$ at $\alpha = 12^\circ$ for the closed slat configuration can be seen as well. This flow behavior is also known from the DU-91-W2-250 airfoil in the clean configuration at higher angles of attack. In contrast to the closed slat configuration, the recirculation area at the lower side of the open slat configuration is getting much smaller with increasing angle of attack. Because of the reduced vortex size at $\alpha = 12^\circ$, a clear gap flow can be seen, and the separation at the trailing edge of the main airfoil with open slat is no longer present. With the definition of the opening angle of attack of the passive-adaptive slat as $\alpha_{open,kin1} = 7^\circ$, the advantages of the closed configuration for low angles of attack and the advantages of the open configuration for high angles of attack can be used.

3 | DESIGN OF THE SLAT KINEMATICS

After the closed and completely open position of the slat have been optimized, the kinematics for an optimal opening and closing have to be designed. First of all, the principle of the passive-adaptive actuation is presented in the following section. Afterwards, the optimization of the passive-adaptive slat kinematics is described. The principle as well as the design of the passive-adaptive slat kinematics are presented for a two-dimensional wind tunnel model, which will be investigated in upcoming measurements at ForWind, University of Oldenburg.

3.1 | Principle of the passive-adaptive actuation

The first idea of the passive-adaptive slat concept is based on the kinematics according to Petrikat²⁰ and Braun.²¹ Braun and Petrikat proposed a kinematics, which extends the slat solely due to the aerodynamic forces acting on it. The slat shall open as soon as a certain lift coefficient is

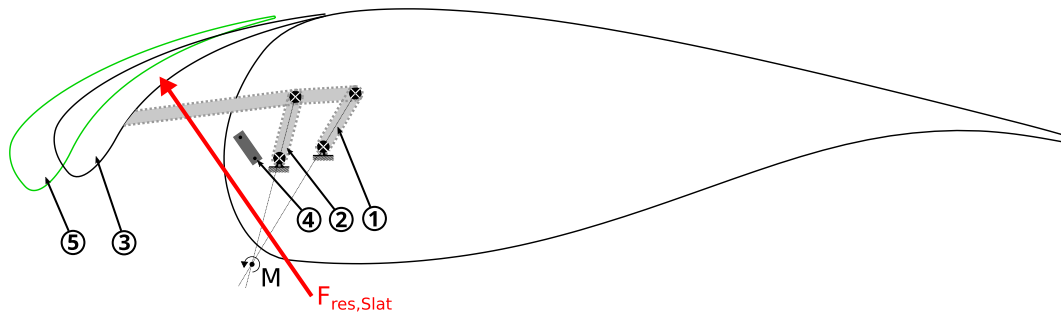


FIGURE 19 Sketch of the principle of the passive-adaptive slat kinematics for the DU-91-W2-250 airfoil with: 1—Lever A, 2—Lever B, 3—Closed Slat, 4—Stopper Element Open Slat Position, 5—Open Slat

TABLE 3 Opening (α_{open}) and closing angle of attacks (α_{close}) of the passive-adaptive slat kinematics

Configuration	α_{open} [°]	α_{close} [°]
Kinematics 1	7	5
Kinematics 2	6	13

reached at a specific angle of attack of the airfoil. The principle of this passive-adaptive actuation can be seen in Figure 19, which sketches the kinematics design for the DU-91-W2-250 airfoil.

The designed kinematics consists of three levers, which are connected by pivot joints. The virtual intersection point of the lever A (1) and lever B (2) forms the instantaneous center of rotation. If this center lies to the left of the resulting aerodynamic force $F_{res, Slat}$ of the slat, an opening moment M is created by the slat. The closed slat (3) is accordingly pulled away from the main profile by the aerodynamic forces. The opening process is limited by a stopper (4), which defines the optimized fully open position of the slat (5). A closing moment arises, when the resulting aerodynamic force of the slat moves to the left of the instantaneous center of rotation. In this case, the slat is pushed to the main profile, and the slot gets closed again. The objectives and thus the guidelines for the kinematics design can be described as follows^{20,21}:

1. A defined slat end position must be achieved.
2. The opening and closing of the slat must be initiated at a previously defined lift coefficient at a certain angle of attack.
3. The opening and closing of the slat must be quick but smooth.
4. When the slat is opening or closing, the flow at the main airfoil must not be disturbed by flow separations.

The design of the passive-adaptive slat kinematics was driven with reference to these guidelines. The defined slat end position, which must be achieved when opening the slat, is the optimized completely open position described in Section 2.6. To reach the defined slat end position and to realize the opening of the slat at the aimed angle of attack, the pivots and levers of the kinematics have to be arranged. The optimization of the slat kinematics levers and pivot points is described in the following section. It has to be mentioned that this first design of the kinematic mechanisms is based on the investigations of Petrikat²⁰ and Braun²¹ and similar to their work was developed without an inclusion of friction and inertia.

3.2 | Optimization of the pivot point positions

To develop a passive-adaptive kinematics, which is opening and closing as designed, the positions of the kinematics pivots have to be optimized in such a way that the corresponding resulting aerodynamic force of the slat passes exactly through the instantaneous center of rotation, both in the closed and in the open slat position at the defined opening (α_{open}) or closing angle of attack (α_{close}). The aim of the kinematics design is thus, that the common point of intersection of lever A and lever B in closed slat position hits the resulting aerodynamic force of the slat $F_{res, Slat, closed, \alpha_{open}}$ and the intersection point of lever A and lever B with open slat position hits the resulting aerodynamic force $F_{res, Slat, open, \alpha_{close}}$. To investigate different opening and closing behaviors of the slat, the angles α_{open} and α_{close} are differently defined for the two designed kinematics (see Table 3).

The opening angle of kinematics 1 is defined larger than the closing angle in order to be able to use a kinematics, in which the slat is for sure completely open for $\alpha > 7^\circ$ and completely closed for $\alpha < 5^\circ$. The slat is therefore in most cases at the closed or optimized open position.

The slight difference between the two opening angles of the two kinematics enables studying on the sensitivity of the opening behavior of the slat. Additionally, the second kinematics should ensure that the slat is completely open at the angle of attack of maximum climb ($\alpha_{c_{l,3/2}/c_{D,max}} = 14^\circ$). The slat should gradually move between the open and closed position with reference to the inflow angle of attack. This is achieved by designing a transition range of the angle of attack, in which the slat is neither completely closed nor completely open. Hence, kinematics 2 is designed that an opening moment occurs on the slat in the closed position for $\alpha > 6^\circ$ and a closing moment occurs on the slat for the completely open position for angles of attack with $\alpha < 13^\circ$. In the range of $\alpha = 6^\circ \dots 13^\circ$, the slat is accordingly in the middle position, whereby it does not open or close abruptly, but is gradually moving with reference to the angle of attack. The slat's position is therefore adapted passively to the inflow and should accordingly adapt to changes in the angle of attack during gusty inflow as well.

The optimized point of rotation S_{rot} around which the whole slat geometry moves is another boundary condition that has to be respected. Furthermore, the movement of the slat should start at the defined closed and stop at the defined completely open position. These boundary conditions reduce the eight coordinates of the pivot points to four free variables whose parameter space has to be examined. The four pivot point coordinates that are changed during the optimization process are sketched in Figure 20 including the position of the spar as further limitation.

Since the entire kinematics has to be installed in the front area of the main airfoil, the limitations of the individual pivot point coordinates are given by the leading edge of the main airfoil, the spar position, and the minimum distance of each pivot defined by the bearing size. The minimum distance of the bearings middle point and therefore the minimum distance of the pivot points was defined as $d_{Bearings}/c = 0.03$. During the optimization of the passive-adaptive slat kinematics, the four pivot point coordinates B_y , C_x , C_y , and D_x were iteratively changed, and the dependent pivot point coordinates A_x , A_y , B_x , and D_y were calculated by the use of the boundary conditions and angle relations between the levers and the slat geometry, which are described more detailed in appendix A1.

Since the four dependent pivot point coordinates (A_x , A_y , B_x , D_y) and thus the instantaneous center of rotation react very sensitive to the variation of the four free parameters (B_y , C_x , C_y , D_x), a Design of Experiment (DOE) was first carried out to investigate the parameter space; 625 parameter variations were carried out, which allow a first overview of potentially favorable pivot positions. Based on the best combination of parameters of the DOE, a SUBPLEX algorithm was again used to find the optimal kinematics design. Hereby, it was important that the fourth goal in Section 3.1 is achieved: Disturbances on the main airfoil flow caused by separations on the slat when opening or closing would reduce the aerodynamic performance of the airfoil. Both the DOE and the SUBPLEX algorithm were therefore carried out on the basis of the climb index at the half-opened slat position for the angles α_{open} and α_{close} .

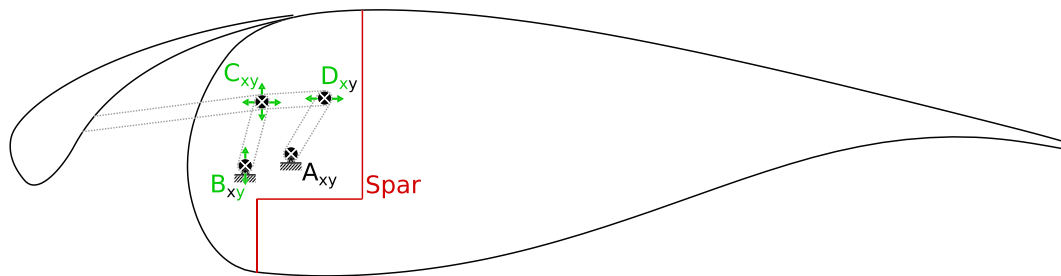


FIGURE 20 Sketch of the passive-adaptive slat kinematics including the pivot point coordinates, which are changed during the optimization (green) with the spar position (red) and the airfoils leading edge as boundaries

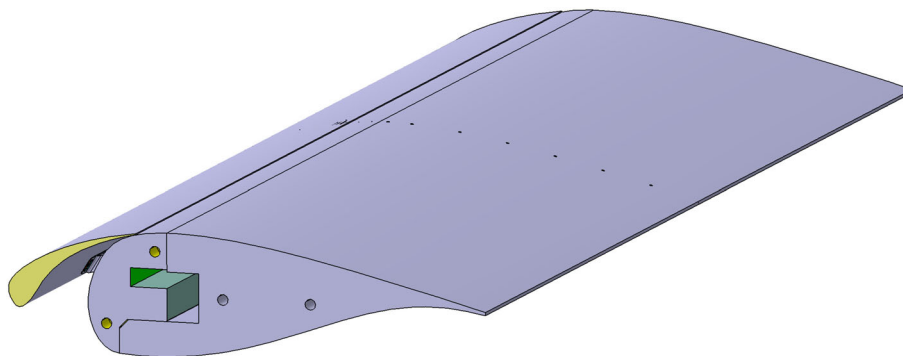


FIGURE 21 Designed airfoil with closed passive-adaptive slat

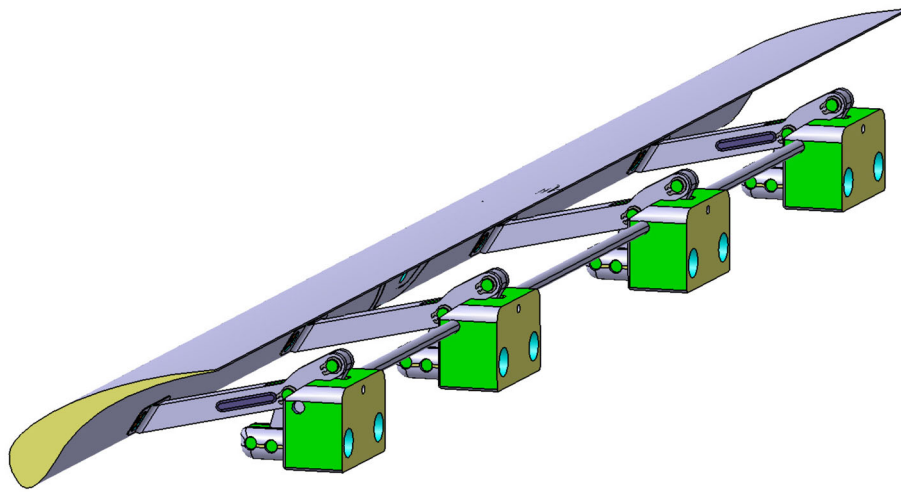


FIGURE 22 Designed airfoil with closed passive-adaptive slat (main airfoil faded out)

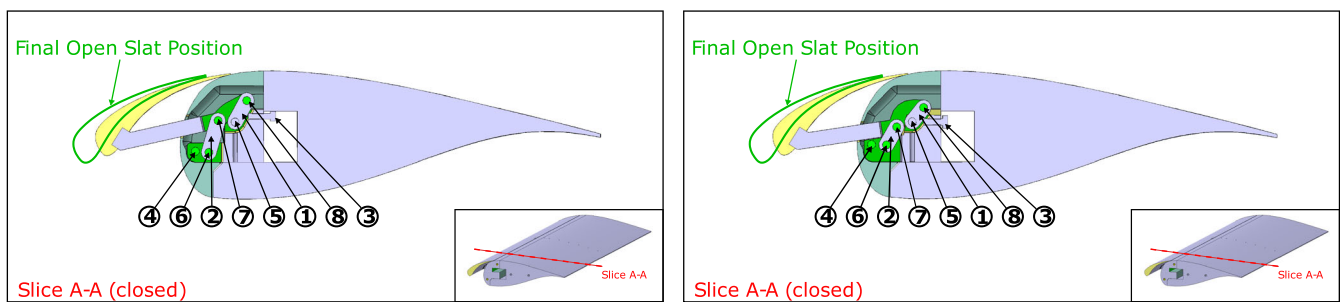


FIGURE 23 Airfoil with closed passive-adaptive slat including kinematics 1 (left) and kinematics 2 (right) as slice of the CAD model for upcoming wind tunnel investigations with: 1—Lever A, 2—Lever B, 3—Stopper Element Closed Slat Position, 4—Stopper Element Open Slat Position, 5—Pivot A, 6—Pivot B, 7—Pivot C, 8—Pivot D

3.3 | Results of the design of the passive-adaptive slat including the two kinematics

After the pivot points of the two kinematics were optimized, a 3D model was generated in CAD. The final geometry of the passive-adaptive slat including the kinematics is shown in Figures 21 and 22.

In Figure 21, the designed airfoil is presented with closed passive-adaptive slat. The model is designed for the use in wind tunnel investigations at ForWind, University of Oldenburg. Therefore, it has a chord length of 0.3 m and a width of 0.8 m. Figure 22 shows the airfoil from the same perspective as in Figure 21 with the main airfoil faded out to make the kinematics blocks inside of the airfoil visible. The airfoil is designed with four identical kinematics blocks, which can be replaced with blocks of differently designed kinematics. The kinematics blocks are connected by a shaft, which guarantees a uniform opening of the four kinematics. In Figures 23–25, the two different kinematics and their differences in the pivot point positions are presented.

As presented in Figure 23, an adjustable screw is used as a stopper (3) for the closed slat position of the kinematics. This screw allows a variation of the closed slat position and thus prevents the kinematics from jamming due to static friction, because the slat does not rest completely on the main airfoil in the closed position. Therefore, the trailing edge of the slat does not touch the main airfoil, which has the further positive effect that the main airfoil cannot be damaged by the slat, if it closes. In addition, the adjustable screw enables investigations of different slat positions and consequently also studies on the aerodynamic behavior of the airfoil with gap variation between the slat and the main airfoil. Furthermore, the position of the closed slat and hence its aerodynamic moment can be varied by changing the closed slat position with the help of the adjusting screw. At the same time, the position of the intersection point of the two kinematics levers can be changed by the adjustable screw. Therefore, the opening moment of the slat and the opening and closing behavior of the slat kinematics can be varied. This is especially necessary because the first design of the kinematics is carried out without an inclusion of friction and inertia. If the friction inside of the kinematics is too high and the slat is not opening, the closed slat position and its opening moment can be changed by the use of the screw.

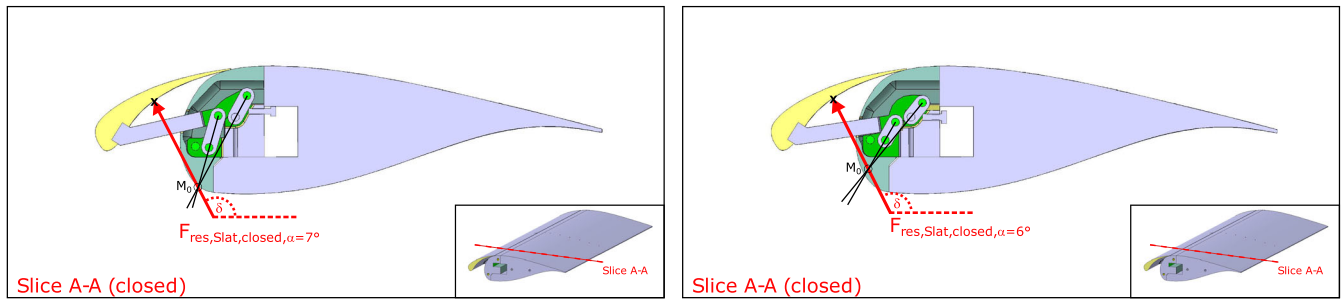


FIGURE 24 Airfoil with closed passive-adaptive slat including the intersection point of lever A and B (M_0) and the resulting aerodynamic force of the slat with application point X for $\alpha = 7^\circ$ with kinematics 1 (left) and $\alpha = 6^\circ$ with kinematics 2 (right)

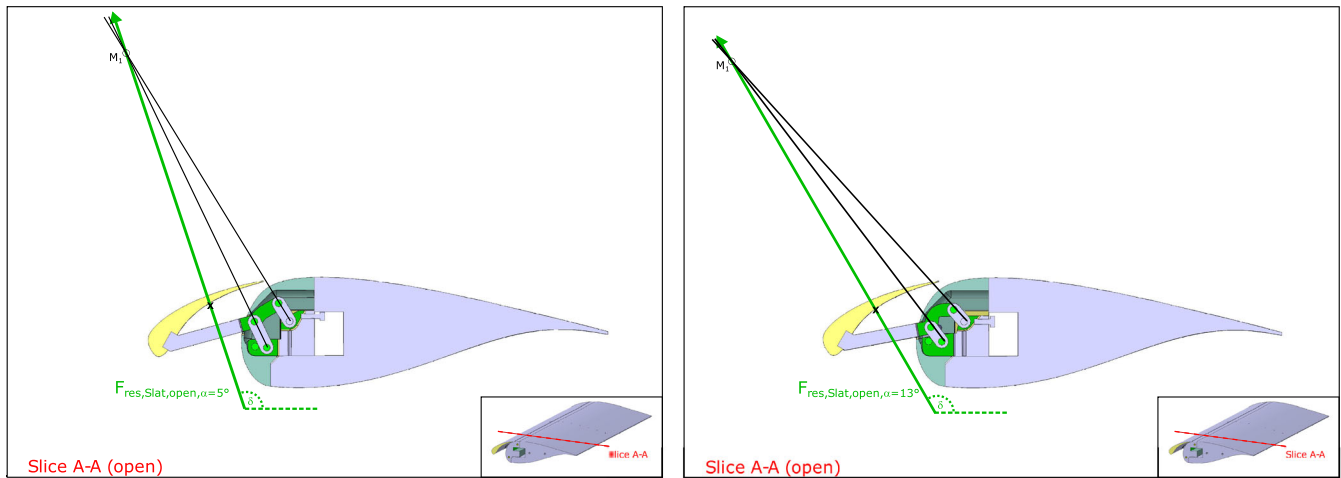


FIGURE 25 Airfoil with open passive-adaptive slat including the intersection point of lever A and B (M_1) and the resulting aerodynamic force of the slat with application point X for $\alpha = 5^\circ$ with kinematics 1 (left) and $\alpha = 13^\circ$ with kinematics 2 (right)

Figures 24 and 25 depict the two designed kinematics in closed and open position together with the resulting aerodynamic force vector at the designated angle of attack for opening and closing. It can be seen that the intersection point of the levers A and B, and therefore, the instantaneous center of rotation of the slat is exactly on the slats resulting aerodynamic force in the closed position for α_{open} and in the open position for α_{close} . The point of application and the direction of the slats resulting aerodynamic force are determined by means of flow simulations (see Section 2.6). In that case, the lever arm of the resulting aerodynamic force and therefore the resulting aerodynamic moment on the airfoils slat with reference to the instantaneous center of rotation are accordingly zero. When the local angle of attack changes, the point of application and the direction of the aerodynamic force of the slat change accordingly. With increasing local angle of attack and a constant inflow velocity, the lift force and the angle of the resulting aerodynamic force δ is increasing, too.²⁰ For $\alpha > \alpha_{open}$, the resulting aerodynamic force thus moves to the right of the kinematics levers intersection point, and an opening moment is arising on the slat. Hence, the slat is opening for $\alpha > \alpha_{open}$ and equivalent closing for $\alpha < \alpha_{close}$. The final position of the slat should be achieved with the help of a stop element as it can be seen in Figure 25. This limits the maximum opening angle of the levers and makes the kinematics come to a halt precisely at the designed open position.

4 | DISCUSSION AND CONCLUSION

This contribution describes the design of a passive-adaptive slat for a DU-91-W2-250 airfoil. The slat is moved on a kinematics only by the air forces acting on it. In the beginning of the design procedure, the slat shape and the final position of the open slat were defined with the use of a RANS-based optimization. The slat geometry was optimized with reference to the maximum lift and the maximum climb index of the airfoil. Afterwards, two different kinematics were developed, which open and close the slat at different defined angles of attack. The designed airfoil including the passive-adaptive slat leads to an increase of the maximum angle of attack by 20° as well as to an increase of the maximum climb index by 20% compared to the original profile. Especially compared to conventional stall delay devices such as VGs, these values are a significant improvement in aerodynamic performance. Hansen et al³⁷ achieved a stall delay of 3° with aerodynamical shaped VGs attached to the DU-91-W2-250

airfoil in comparable flow conditions. Furthermore, the DU-91-W2-250 airfoil with closed passive-adaptive slat for $\alpha < 7^\circ$ and with open passive-adaptive slat for $\alpha > 9^\circ$ achieves a higher climb index and therefore a better aerodynamic performance than the same airfoil with fixed integrated slat. Accordingly, the positive effects of a movable slat could be clearly demonstrated.

There is potential for improvement since the airfoil with a movable slat has a lower drag coefficient than the airfoil with a fixed slat but especially for small angles of attack still a higher drag coefficient than the original profile. As Steiner et al¹⁷ pointed out, the drag as well as the lift coefficient of the designed airfoil could be improved by designing the slat and the main airfoil together. In the next step, the aerodynamic behavior of the designed airfoil and its passive-adaptive slat will be investigated in a wind tunnel. During the wind tunnel tests, the numerical simulations will be validated, and the opening and closing behavior of the slat will be investigated. In addition, it is important to investigate how the passive-adaptive slat behaves in gusty inflows as well as in a rotating system, when installed at a wind turbine's rotor blade. Furthermore, the influence of such a movable slat on the structural design of a rotor blade has to be explored.

A key aspect of the upcoming researches will be to investigate how such a passive-adaptive slat can be integrated into a full-scale model of a rotor blade. As a first orientation, the following procedure should be followed: The design of the shape and position of the 3D passive-adaptive slat can be fulfilled equivalent to the procedure for the development of the 2D passive-adaptive slat of the DU-91-W2-250 airfoil (see Section 2). With the use of 2D RANS-based optimization, the section profiles of the rotor blade including the passive-adaptive slat should be designed at various section positions. In the course of this, studies should be carried out on the optimal spanwise position of the slat at the rotor blade. Subsequently, the optimized full-scale geometry of the rotor blade including the passive-adaptive slat should be investigated using 3D RANS simulations, and the slat shape including its side edges as well as the slat position should be adjusted if necessary. When designing the passive-adaptive slat kinematics including the slat's opening and closing angle of attack, it is important to design the mechanical lever's virtual intersection point with reference to the resulting aerodynamic force application point as well as with reference to the aerodynamic force resultant of the 3D slat. Accordingly, each spanwise mechanism should be designed with reference to one common pivot point around which the whole slat geometry is moving around. The optimization procedure can be done in an equivalent way to the procedure presented in Section 3. Hereby, the spanwise spar position as well as the local twist angle of the full-scale rotor blade should be used as a boundary condition. As in the wind tunnel model, it is essential for the functioning of the passive-adaptive slat mechanism that the spanwise kinematics blocks are connected by a shaft (see Section 3.3). Otherwise, the mechanisms will not open simultaneously and the slat will jam. In addition, it is also important to create a readjustment option inside of the 3D mechanisms such as an adjusting screw (see Section 3.3) with which the position of the slat and the position of the mechanical levers can be adjusted. In front of the integration of the slat in the full-scale blade, a weight estimation of the slat should also be made in order to correctly dimension the slat mechanism itself and the spanwise number of mechanisms. When designing the passive-adaptive slat for a full-scale model, the work of Rudolph⁴⁰ and Niu⁴¹ should be considered. They have discussed several mechanisms for high-lift devices on commercial aircrafts and give some guidelines that have to be considered during the development of a 3D high-lift device including fail-safe-strategies.

Another aspect that needs to be investigated is the effect of the designed leading-edge slat on noise generation. From aircraft design, it is known that slats are a dominant source of airframe noise especially during aircraft landing.⁴²⁻⁴⁴ Furthermore, Suryadi et al⁴⁵ investigated the noise generation of a rigid inboard slat at a wind turbine using DLRs numerical prediction toolchain FRPM/FMCAS (Fast Random Particle Mesh/Fast Multipole Code for Acoustic Shielding). According to their research, the slat noise contributions are negligible only for small wind velocities. Especially in the fully-load region, the slat contributes an additional 1.5 dBA to the A-rated overall sound pressure level of the rotor blades. Hence, the noise generation of the designed passive-adaptive slat will be analyzed in detail with the help of upcoming aeroacoustic measurements at ForWind, University of Oldenburg. Based on the results of the aeroacoustic measurements, noise reduction techniques can be developed for the designed airfoil, and the optimization procedure can be improved with reference to noise generation. The additional noise emission generated by the passive-adaptive slat should also be investigated in more detail using highly resolved numerical methods. In the course of this, the influence of the laminar-turbulent transition on the aerodynamic performance of the airfoil with slat compared to the clean DU-91-W2-250 airfoil without slat device should be further investigated. Within this context, sensitivity studies about the robustness of the passive-adaptive slat kinematics against leading edge contamination needs to be done. Since the range of application of the passive-adaptive slat kinematics is mainly designed for small angles of attack (see Section 3), the functioning of the passive-adaptive mechanism should not be affected by a leading edge contamination, but this remains to be seen in further investigations.

ACKNOWLEDGEMENTS

This work has been funded by the German Ministry of Economic Affairs and Energy (BMWi) on decision of the German Parliament in the frame of the SmartBlades 2.0 project (funding reference no. 0324032D). Furthermore, especially the CAD model of kinematics 1 was designed in consultation with the Deharde GmbH. The first wind tunnel investigations of the behavior of the designed geometry were carried out by Piyush Singh of ForWind, University of Oldenburg, in cooperation with the authors of this research article.

CONFLICT OF INTEREST

The authors declare that they have no conflicts of interest.

PEER REVIEW

The peer review history for this article is available at <https://publons.com/publon/10.1002/we.2696>.

DATA AVAILABILITY STATEMENT

The access to the data is restricted, which is why the research data are not shared. For further information about the data that support the findings of this study, the corresponding author can be contacted.

ORCID

Florian N. Schmidt  <https://orcid.org/0000-0002-5537-7214>

Jochen Wild  <https://orcid.org/0000-0002-2303-3214>

REFERENCES

1. Spinato F, Tavner PJ, van Bussel GJW, Koutoulako E. Reliability of wind turbine subassemblies. *IET Renew Power Gener.* 2009;3(4):387. <https://doi.org/10.1049/iet-rpg.2008.0060>
2. Aramendia I, Fernandez Gamiz U, Ramos Hernanz JA, Sancho J, Lopez Guede JM, Zulueta E. Flow Control Devices for Wind Turbines. *Energy Harvesting and Energy Efficiency, Lecture Notes in Energy*, Vol. 37. Springer; 2017. https://doi.org/10.1007/978.3.319.49875-1_21
3. Pechlivanoglou G Passive and Active Flow Control Solutions for Wind Turbine Blades. Dissertation. University of Berlin, Germany; 2013. <https://doi.org/10.14279/depositonce-3487>
4. Chow R, van Dam CP. Inboard Stall and Separation Mitigation Techniques on Wind Turbine Rotors. *49th AIAA Aerospace Sciences Meeting Including the New Horizons Forum and Aerospace Exposition*. Florida, United States, 2011. <https://doi.org/10.2514/6.2011-152>
5. Barlas TK, van Kuik GAM. Review of state of the art in smart rotor control research for wind turbines. *Progress Aerosp Sci.* 2010;46(1):1-27. <https://doi.org/10.1016/j.paerosci.2009.08.002>
6. Taylor HD. The Elimination of Diffuser Separation by Vortex Generators. Report No. R-4012-3, United Aircraft Corporation, Moscow, Russia; 1947.
7. Godard G, Stanislas M. Control of a decelerating boundary layer. Part 1: optimization of passive vortex generators. *Aerosp Sci Technol.* 2006;10(3):181-191. <https://doi.org/10.1016/j.ast.2005.11.007>
8. Velte CM, Hansen MOL, Meyer KE, Fuglsang P. Evaluation of the performance of vortex generators on the DU91-W2-250 profile using stereoscopic PIV. In: *Proceedings of the 12th World Multi-Conference on Systemics, Cybernetics and Informatics (WMSCI 2008)*, Vol. 2. Orlando, Florida, USA; 2008:263-267.
9. Gao L, Zhang H, Liu Y, Han S. Effects of vortex generators on a blunt trailing-edge airfoil for wind turbines. *Renew. Energy.* 2015;76:303-311. <https://doi.org/10.1016/j.renene.2014.11.043>
10. Øye S. The effect of vortex generators on the performance of the ELKRAFT 1000 kw turbine. In: *Aerodynamics of Wind Turbines: 9th IEA Symposium*, Stockholm, Sweden; 1995:9-14.
11. Baldacchino D, Manolesos M, Ferreira C, et al. Experimental benchmark and code validation for airfoils equipped with passive vortex generators. In: *Journal of Physics: Conference Series*, 753, 022 002, Munich, Germany; 2016. <http://stacks.iop.org/1742-6596/>
12. Smith AMO & Smith AMO High-lift aerodynamics. *J Aircr.* 1975;12(6):501-530. <https://doi.org/10.2514/3.59830>
13. Zahle F, Gaunaa M, Sørensen NN, Bak C. Design and Wind Tunnel Testing of a Thick, Multi-Element High-Lift Airfoil. *EWEA 2012 - European Wind Energy Conference and Exhibition*, Copenhagen, Denmark; 2012.
14. Pechlivanoglou G, Nayeri CN, Paschereit C. Fixed Leading Edge Auxiliary Wing as a Performance Increasing Device for HAWT Blades. In: *Proceedings of the Deutscher Windenergie Kongress (DEWEK)*. Bremen, Germany; 2010.
15. Gaunaa M, Zahle F, Sørensen NN, Bak C. Quantification of the effects of using slats on the inner part of a 10MW rotor. Poster session presented at *EWEA 2012 - European Wind Energy Conference and Exhibition*. Copenhagen, Denmark, PO. ID 303; 2012.
16. Manso Jaume A, Wild J. Aerodynamic design and optimization of a high-lift device for a wind turbine airfoil. *New Results in Numerical and Experimental Fluid Mechanics*, Vol. X. Berlin Heidelberg, Germany: Springer; 2016:859-869. <https://doi.org/10.1007/978-3-319-27279-5>
17. Steiner J, Viré A, Benetti F, Timmer N, Dwight R. Parametric slat design study for thick base airfoils at high Reynolds Numbers. *Wind Energy Sci.* 2020; 5(3):1075-1095. <https://doi.org/10.5194/wes-5-1075-2020>
18. Young TM, Seabridge A. Aerodynamic fundamentals. In: *Performance of the Jet Transport Airplane*. Ireland: Wiley University of Limerick; 2018:71.
19. Singh P, Neuhaus L, Huxdorf O, et al. Experimental investigation of an active slat for airfoil load alleviation. *J Renew Sustain Energy*. Submitted.
20. Petrikat K. Untersuchungen an festen und selbsttätig öffnenden Vorflügeln im Wasserkanal der Gerhard Fieseler Werke. *Jahrbuch der deutschen Luftfahrtforschung*, Vol. 1. Kassel, Germany; 1940:248-264.
21. Braun. Untersuchungen von Vorflügelkinematiken, Messerschmidt report 33/41. Augsburg, Germany; 1941.
22. Brezillon J, Abu-Zurayk M. Aerodynamic inverse design framework using discrete adjoint method. *New Results in Numerical and Experimental Fluid Mechanics VIII*, Vol. 121. Berlin Heidelberg, Germany; Springer; 2012:489-496. <https://doi.org/10.1007/978-3-642-35680-358>
23. Maxwell FR. Airplane Wing. Patent US-2,381,678, Pennsylvania USA; 1945.
24. Brodersen O, Hepperle M, Ronzheimer A, Rossow CC, Schöning B. The parametric grid generation system MegaCads. In: *Proc. 5th International Conference on Numerical Grid Generation in Computational Field Simulations*. NSF Engineering Research Center Mississippi State University; 1996:353-362.
25. Wild J. Numerische Optimierung von zweidimensionalen Hochauftriebskonfigurationen durch Lösung der Navier-Stokes-Gleichungen. Dissertation: University of Braunschweig, Germany; 2001. DLR-FB-2011-11.
26. Sevinc A, Rosemeier M, Bätge M, et al. IWES WIND TURBINE IWT-7.5-164 REV. 2.5. Technical Report, Germany, Fraunhofer IWES, Fraunhofer Institute for Wind Energy Systems IWES and Leibnitz Universität Hannover; 2017.
27. Kroll N, Eisfeld B, Bleecke HM. The Navier-Stokes Code FLOWer. In: *Vol. 71 of Notes on Numerical Fluid Mechanics*. Braunschweig, Germany: Vieweg; 1999:58-71.

28. Timmer WA, van Rooij RPJOM. Summary of the Delft University Wind Turbine Dedicated Airfoils. *J Solar Energy Eng.* 2003;125:488-496. <https://doi.org/10.1115/1.1626129>
29. Van Rooij RPJOM, Timmer WA. Roughness sensitivity considerations for thick rotor blade airfoils. *J Solar Energy Eng.* 2003;125(4):468-478. <https://doi.org/10.1115/1.1624614>
30. Rogowski K, Hansen MOL, Hansen R, Piechna J, Lichota P. Detached eddy simulation model for the DU-91-W2-250 airfoil. *J Phys: Conf Ser.* 2018; 1037:022019. <https://doi.org/10.1088/1742-6596/1037/2/022019>
31. Sreejith BK, Sathyabhama A. Numerical study on effect of boundary layer trips on aerodynamic performance of E216 airfoil. *Int J Eng Sci Technol.* 2018;21(1):77-88. <https://doi.org/10.1016/j.jestch.2018.02.005>
32. Manso Jaume A, Wild J, Homeyer T, Hölling M, Peinke J. Design and wind tunnel testing of a leading edge slat for a wind turbine airfoil. In: Proceedings of the Deutscher Windenergie Kongress (DEWEK). Bremen, Germany; 2015.
33. Rowan T. Functional Stability Analysis of Numerical Algorithms. *Dissertation:* University of Texas at Austin USA; 1990.
34. Daniele E, Stoevesandt B, Rosermeier M, Bleich O. 3D steady simulation of a 7.5 MW wind turbine with OpenFOAM. In: European Fluid Mechanics Conference, Vol. 10. Copenhagen, Denmark; 2014. <https://doi.org/10.13140/RG.2.2.26000.92160>
35. Teßmer J, Icpinar C, Sevenic A, et al. Schlussbericht Smart Blades: 01.12.2012-30.04.2016. <https://doi.org/10.2314/GBV:871472740>; 2016
36. Imiela M. Prediction of aerodynamic loads for the SB80 rotor. SmartBlades Conference, Stade, Germany; 2016.
37. Hansen MOL, Velte CM, Øye S, et al. Aerodynamically shaped vortex generators. *Wind Energy.* 2015;19(3). <https://doi.org/10.1002/we.1842>
38. Boufferrouk A, Chernyshenko SI. Stabilisation of a Trapped Vortex for Enhancing Aerodynamic Flows. In: 15th Australasian Fluid Mechanics Conference, Sydney, Australia; 2004. AFMC00193.
39. Kasper WA. Aircraft wing with vortex generation. Patent US-3,831,885, Washington USA; 1974.
40. Rudolph PKC. High-Lift Systems on Commercial Subsonic Airliners, NASA Contractor Report 4746; 1996.
41. Niu MC-Y. *Airframe Structural Design.* Hong Kong: Conmilit Press Ltd; 1997;303-357.
42. Dobrzynski W, Gehlhar B, Buchholz H. Model and full scale high lift wing wind tunnel experiments dedicated to airframe noise reduction. *Aerosp Sci Technol.* 2001;5(1):27-33. [https://doi.org/10.1016/S1270-9638\(00\)01079-8](https://doi.org/10.1016/S1270-9638(00)01079-8)
43. Molin N, Molin N. Airframe noise modeling and prediction. *CEAS Aeronaut J.* 2019;10(1):11-29. <https://doi.org/10.1007/s13272-019-00375-4>
44. Pott-Pollenske M, Wild J, Bertsch L. Aerodynamic and Acoustic Design of Silent Leading Edge Devices. In: 20th AIAA/CEAS Aeroacoustics Conference, Atlanta, GA, USA; 2014. <https://doi.org/10.2514/6.2014-2076>
45. Suryadi A, Schmidt FN, Appel C, Reiche N, Ewert R, Herr M, Wild J. FRPM/FMCAS Application for Prediction of Wind Turbine Noise. In: Wind Energy Science Conference (WESC) 2021, Conference Proc., European Academy of Wind Energy (eawe); 2021.

How to cite this article: Schmidt FN, Wild J. Development of a passive-adaptive slat for a wind turbine airfoil. *Wind Energy.* 2021;1-25. doi:10.1002/we.2696

APPENDIX A: Determination of the dependent pivot point coordinates with the help of the geometric boundary conditions

The leading edge including the kinematics and the parameter names that are used in the equations are sketched in Figure A.1 and Figure A.2. Hereby, the four pivot points are defined as follows:

$$A = A_x * \vec{e}_x + A_y * \vec{e}_y \quad (\text{A1})$$

$$B = B_x * \vec{e}_x + B_y * \vec{e}_y \quad (\text{A2})$$

$$C = C_x * \vec{e}_x + C_y * \vec{e}_y \quad (\text{A3})$$

$$D = D_x * \vec{e}_x + D_y * \vec{e}_y \quad (\text{A4})$$

The indices of the pivot points are describing the position of the slat with closed as index “0” and completely open as index “1.” Furthermore, in Figure A.1, the relation between the pivot points C and D and the optimized point of rotation S_{rot} becomes clear. The perpendicular bisector of the straight line that connects C_0 and C_1 runs exactly through pivot point B and the perpendicular bisector of the straight line that connects D_0 and D_1 runs exactly through pivot point A. Additionally, the rotation point S_{rot} is the virtual intersection point of these two perpendicular bisectors. The angle ϕ between the two perpendicular bisectors is the angle the whole slat geometry is rotated around the point S_{rot} to reach the completely open position.

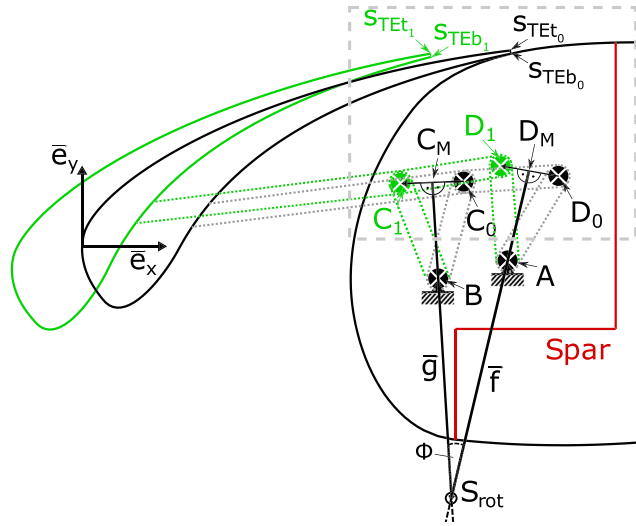


FIGURE A.1 Leading edge of the designed airfoil with a sketch of the passive-adaptive slat kinematics including the pivot points in closed (index “0”) and open (index “1”) position and the perpendicular bisector between the points C_0/C_1 and D_0/D_1 , which intersection point is the optimized slat rotation point S_{rot}

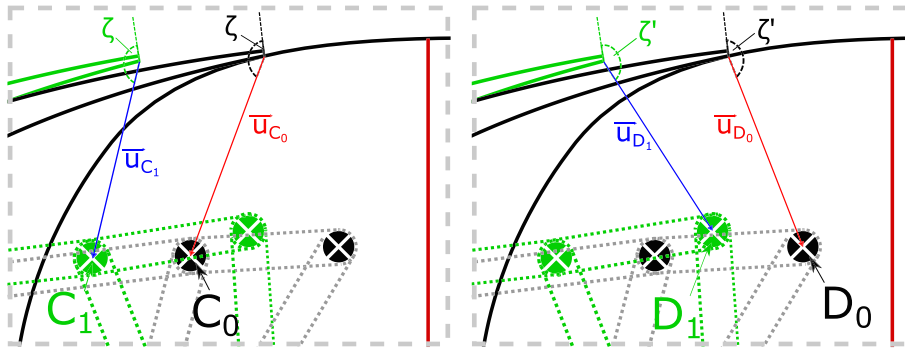


FIGURE A.2 Detail of the sketched passive-adaptive slat kinematics including the vector connecting the corner of the trailing edge of the closed slat with C_0/D_0 (red) and the corner of the trailing edge of the open slat with C_1/D_1 (blue)

When looking at the vectors in Figure A.2, it also becomes clear that the definition of C_{x_0} and C_{y_0} immediately defines point C_1 . The angle ζ is the same for the vectors with closed (red) and open slat (blue). Furthermore, the length of the vectors is equal with the following:

$$|\vec{u}_{C_0}| = |\vec{u}_{C_1}| \quad (\text{A5})$$

Equivalently, the angle ζ' between the trailing edge of the slat and the vector \vec{u}_D is the same for the closed and for the open slat position. The length of the vectors in Figure A.2 is also related with the following:

$$|\vec{u}_{D_0}| = |\vec{u}_{D_1}| \quad (\text{A6})$$

With the acute angle χ_0 between the closed slats trailing edge and the axis of \vec{e}_x , the coordinates of point C_1 can be determined with the relation:

$$\chi_1 = \phi - \chi_0 \quad (\text{A7})$$

$$C_1 = (S_{TEb,x_1} - \cos(\chi_1) * |\vec{u}_{C_1}|) * \vec{e}_x + (S_{TEb,y_1} - \sin(\chi_1 - \zeta) * |\vec{u}_{C_1}|) * \vec{e}_y \quad (\text{A8})$$

An equivalent system of equations results for the determination of point D_1 with the slat open:

$$D_1 = (s_{TEb,x_1} + \cos(\chi_1 - \zeta') * |\overrightarrow{u_{D_1}}|) * \overrightarrow{e_x} + (s_{TEb,y_1} - \sin(\chi_1 - \zeta') * |\overrightarrow{u_{D_1}}|) * \overrightarrow{e_y} \quad (A9)$$

Since D_{y_0} and therefore $\overrightarrow{u_{D_0}}$ and $\overrightarrow{u_{D_1}}$ are not known, the relation between the two points D_0 and D_1 as well as their relation to the rotation point S_{rot} and C_0 and C_1 is necessary to determine the position of point D_1 . These relations can be described with the following:

$$C_M = (C_{x_0} + 0.5 * (C_{x_1} - C_{x_0})) * \overrightarrow{e_x} + (C_{y_0} + 0.5 * (C_{y_1} - C_{y_0})) * \overrightarrow{e_y} \quad (A10)$$

$$D_M = (D_{x_0} + 0.5 * (D_{x_1} - D_{x_0})) * \overrightarrow{e_x} + (D_{y_0} + 0.5 * (D_{y_1} - D_{y_0})) * \overrightarrow{e_y} \quad (A11)$$

The perpendicular bisectors \overrightarrow{g} and \overrightarrow{f} in Figure A.1 can be described with the following equation:

$$\overrightarrow{g} = \overrightarrow{m_g} * r_g + \overrightarrow{n_g} \quad \text{with } r_g \in \mathbb{R} \quad (A12)$$

$$\overrightarrow{f} = \overrightarrow{m_f} * r_f + \overrightarrow{n_f} \quad \text{with } r_f \in \mathbb{R} \quad (A13)$$

Furthermore, the coordinates of the support vector \overrightarrow{n} and of the direction vector \overrightarrow{m} that are describing the lines \overrightarrow{g} and \overrightarrow{f} can be formulated as follows:

$$\overrightarrow{m_g} = (S_{rot,x} - C_{M,x}) * \overrightarrow{e_x} + (S_{rot,y} - C_{M,y}) * \overrightarrow{e_y} \quad (A14)$$

$$\overrightarrow{m_f} = (S_{rot,x} - D_{M,x}) * \overrightarrow{e_x} + (S_{rot,y} - D_{M,y}) * \overrightarrow{e_y} \quad (A15)$$

$$\overrightarrow{n_g} = C_{M,x} * \overrightarrow{e_x} + C_{M,y} * \overrightarrow{e_y} \quad (A16)$$

$$\overrightarrow{n_f} = D_{M,x} * \overrightarrow{e_x} + D_{M,y} * \overrightarrow{e_y} \quad (A17)$$

With the condition that the resulting force vector of the slat $F_{res,Slat,closed,\alpha_{open}}$ shall exactly go through the intersection of kinematics levers A and B (instantaneous pole M_0) with the slat closed and the condition that the resulting force vector of the slat $F_{res,Slat,open,\alpha_{close}}$ shall exactly go through the intersection of kinematics levers A and B (instantaneous pole M_1) with the slat open, the coordinates of the pivot points B and finally A can be calculated. For a better understanding of the variables in the following equations, the intersection point of the levers A and B and the resulting aerodynamic force of the slat are sketched for the closed as well as the open slat in Figure A.3.

As mentioned before, the perpendicular bisector described by \overrightarrow{g} is going through pivot point B. Furthermore, the lines described by $\overrightarrow{b_0}$ and by $\overrightarrow{b_1}$ have an intersection point at pivot point B, too, which means that pivot point B can be determined by calculating this intersection point. The lines described by \overrightarrow{a} and \overrightarrow{b} that are sketched in Figure A.3 can be described as follows:

$$\overrightarrow{a_0} = \overrightarrow{m_{a_0}} * r_{a_0} + \overrightarrow{n_{a_0}} \quad \text{with } r_{a_0} \in \mathbb{R} \quad (A18)$$

$$\overrightarrow{a_1} = \overrightarrow{m_{a_1}} * r_{a_1} + \overrightarrow{n_{a_1}} \quad \text{with } r_{a_1} \in \mathbb{R} \quad (A19)$$

$$\overrightarrow{b_0} = \overrightarrow{m_{b_0}} * r_{b_0} + \overrightarrow{n_{b_0}} \quad \text{with } r_{b_0} \in \mathbb{R} \quad (A20)$$

$$\overrightarrow{b_1} = \overrightarrow{m_{b_1}} * r_{b_1} + \overrightarrow{n_{b_1}} \quad \text{with } r_{b_1} \in \mathbb{R} \quad (A21)$$

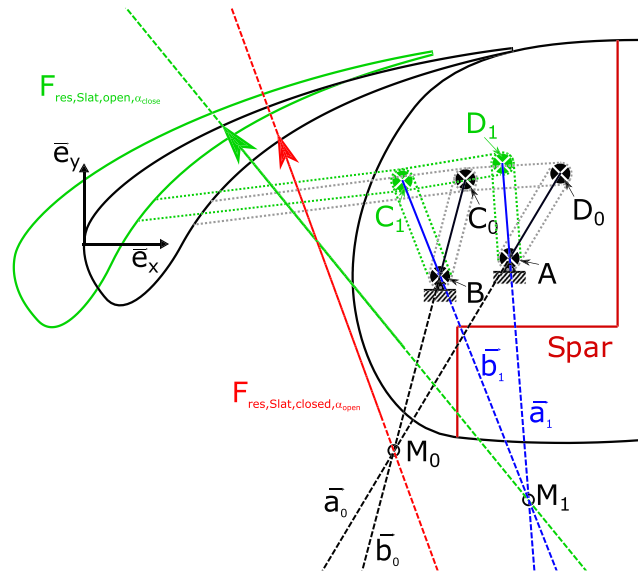


FIGURE A.3 Sketch of the passive-adaptive slat kinematics including the pivot points and the intersection point M of lever A and lever B for the closed (index “0”) and completely open slat position (index “1”), which are designed to go exactly through the resulting aerodynamic force of the slat at the defined angle of attack

The coordinates of the support vector \vec{n} and of the direction vector \vec{m} that are describing the lines \vec{a} and \vec{b} for the closed and open slat position can be formulated with the help of the instantaneous poles M_0 and M_1 as follows:

$$\vec{m}_{b_0} = (M_{x_0} - C_{x_0}) * \vec{e}_x + (M_{y_0} - C_{y_0}) * \vec{e}_y \quad (\text{A22})$$

$$\vec{m}_{b_1} = (M_{x_1} - C_{x_1}) * \vec{e}_x + (M_{y_1} - C_{y_1}) * \vec{e}_y \quad (\text{A23})$$

$$\vec{m}_{a_0} = (M_{x_0} - D_{x_0}) * \vec{e}_x + (M_{y_0} - D_{y_0}) * \vec{e}_y \quad (\text{A24})$$

$$\vec{m}_{a_1} = (M_{x_1} - D_{x_1}) * \vec{e}_x + (M_{y_1} - D_{y_1}) * \vec{e}_y \quad (\text{A25})$$

$$\vec{n}_{b_0} = C_{x_0} * \vec{e}_x + C_{y_0} * \vec{e}_y \quad (\text{A26})$$

$$\vec{n}_{b_1} = C_{x_1} * \vec{e}_x + C_{y_1} * \vec{e}_y \quad (\text{A27})$$

$$\vec{n}_{a_0} = D_{x_0} * \vec{e}_x + D_{y_0} * \vec{e}_y \quad (\text{A28})$$

$$\vec{n}_{a_1} = D_{x_1} * \vec{e}_x + D_{y_1} * \vec{e}_y \quad (\text{A29})$$

Finally, the pivot point B can be found by calculating the intersection point of the line that is described by vector \vec{g} and the line that is described by vector \vec{b}_1 .

$$\vec{g} = \vec{b}_1 \quad (\text{A30})$$

$$(S_{rot} - C_M) * r_g + C_M = (M_1 - C_1) * r_{b_1} + C_1 \quad (\text{A31})$$

The resulting equation to calculate the pivot point B is as follows:

$$\vec{B} = ((S_{rot,x} - C_{M,x}) * r_g + C_{M,x}) * \vec{e}_x + ((S_{rot,y} - C_{M,y}) * r_g + C_{M,y}) * \vec{e}_y \quad (A32)$$

$$\text{with } r_g = \left(\frac{C_{M,x} - C_{x1}}{M_{x1} - C_{x1}} - \frac{C_{M,y} - C_{y1}}{M_{y1} - C_{y1}} \right) / \left(\frac{S_{rot,y} - C_{M,y}}{M_{y1} - C_{y1}} - \frac{S_{rot,x} - C_{M,x}}{M_{x1} - C_{x1}} \right) \quad (A33)$$

Equivalent, the pivot point A can be found by calculating the intersection point of the line that is described by vector \vec{f} and the line that is described by vector \vec{a}_0 .

$$\vec{f} = \vec{a}_0 \quad (A34)$$

$$(S_{rot} - D_M) * r_f + D_M = (M_0 - D_0) * r_{a_0} + D_0 \quad (A35)$$

The resulting equation to calculate the pivot point A is as follows:

$$\vec{A} = ((S_{rot,x} - D_{M,x}) * r_f + D_{M,x}) * \vec{e}_x + ((S_{rot,y} - D_{M,y}) * r_f + D_{M,y}) * \vec{e}_y \quad (A36)$$

$$\text{with } r_f = \left(\frac{D_{M,x} - D_{x_0}}{M_{x_0} - D_{x_0}} - \frac{D_{M,y} - D_{y_0}}{M_{y_0} - D_{y_0}} \right) / \left(\frac{S_{rot,y} - D_{M,y}}{M_{y_0} - D_{y_0}} - \frac{S_{rot,x} - D_{M,x}}{M_{x_0} - D_{x_0}} \right) \quad (A37)$$